Resting-state directed brain connectivity patterns in adolescents from source-reconstructed EEG signals based on information flow rate

Dionissios T. Hristopulos[1]*, **Arif Babul**[2†], **Shazia Babul**[3†], **Leyla R. Brucar**[4†], **Naznin Virji-Babul**[4†]

*For correspondence:
dchristopoulos@isc.tuc.gr (DTH)

[†]These authors contributed equally to this work
[‡]These authors also contributed equally to this work

[1]Telecommunication Systems Research Institute and School of Mineral Resources Engineering, Technical University of Crete, Chania, Crete, Greece; [2]Department of Physics and Astronomy, University of Victoria, Victoria, British Columbia, Canada; [3]Rockefeller College, Princeton University, Princeton, New Jersey, USA; [4]Department of Physical Therapy, Faculty of Medicine, Djavad Mowafaghian Centre for Brain Health, University of British Columbia, Vancouver, British Columbia, Canada

Abstract Quantifying the brain's effective connectivity offers a unique window onto the causal architecture coupling the different regions of the brain. Here, we advocate a new, data-driven measure of directed (or effective) brain connectivity based on the recently developed information flow rate coefficient. The concept of the information flow rate is founded in the theory of stochastic dynamical systems and its derivation is based on first principles; unlike various commonly used linear and nonlinear correlations and empirical directional coefficients, the information flow rate can measure causal relations between time series with minimal assumptions. We apply the information flow rate to electroencephalography (EEG) signals in adolescent males to map out the directed, causal, spatial interactions between brain regions during resting-state conditions. To our knowledge, this is the first study of effective connectivity in the adolescent brain. Our analysis reveals that adolescents show a pattern of information flow that is strongly left lateralized, and consists of short and medium ranged bidirectional interactions across the frontal-central-temporal regions. These results suggest an intermediate state of brain maturation in adolescence.

Introduction

The brain is a complex entity comprising widely distributed but highly interconnected regions, the dynamic interplay of which is essential for brain function. Establishing how activity is coordinated across these regions to give rise to organized (higher order) brain functions ranks as one of the key challenges in neuroscience. Various measures of brain connectivity are in use for this purpose as discussed in (*Friston, 1994*; *Horwitz, 2003*; *Sporns, 2011*; *Rubinov and Sporns, 2010*; *Friston, 2011*; *Cohen, 2014*) and references therein. Structural measures are based on confirmed anatomical connections between brain regions. Functional measures involve dynamically changing, linear or nonlinear, non-directional coefficients of statistical dependence (e.g., correlation, covariance, phase-locking values, coherence) that may appear between structurally unconnected regions. Effective brain connectivity measures capture directionally dependent interactions between different brain regions and aim to identify causal mechanisms in neural processing. In the following, we use the terms "effective" and "directed" connectivity interchangeably. We refer readers to *Sakkalis* (*2011*) and *Bastos and Schoffelen* (*2015*) for recent reviews of functional and effective connectivity measures in the brain. Herein, we investigate effective connectivity patterns as revealed by electroencephalography (EEG) recordings (*Van de Ville et al., 2010*) of scalp electromagnetic fields following source-space reconstruction.

The multichannel EEG signals, which are thought to reflect activity in the underlying brain regions, offer a convenient window into the temporal dynamics of the corresponding brain-scale neuronal networks. EEG studies have been extensively used to infer the nature of the functional connectivity —- i.e. the linear or nonlinear statistical interdependence between the electrical activity in the different brain regions (*Stam and Van Straaten, 2012*) — during resting state or during task related activities. In this paper, we focus our attention on the former.

The resting-state or persistent background activity, previously dismissed as background noise, has been shown to comprise coherent patterns of functional connectivity and appears to play a critical role in mediating complex functions such as memory, language, speech and emotional states (*Raichle et al., 2001*; *Raichle and Mintun, 2006*). There has been considerable progress in mapping out the key resting-state functional brain networks as well as tracking how they change over development. These functional connectivity studies indicate that the resting-state brain networks are sparsely connected in childhood (*Fair et al., 2008*) and evolve towards increased connectivity in adolescence (*Smit et al., 2012*). However, a more complete description remains elusive. For one, very little is known about how information flows within these networks, and how these flow patterns change with maturation.

Several different approaches are in use for quantifying the brain's effective connectivity. Structural approaches such as Structural Equation Modeling (SEM) (*McLntosh and Gonzalez-Lima, 1994*) and Dynamic Causal Modeling (*Friston et al., 2003*) involve a neuranatomical model of the brain and a connectivity model. Other measures are data-driven and involve a statistical model, such as Granger-causality-based methods (*Kamiński et al., 2001*; *Hesse et al., 2003*; *Roebroeck et al., 2005*; *Ding et al., 2006*; *Bressler and Seth, 2011*; *Seth et al., 2015*). A different data-driven approach involves information theoretic measures, like transfer entropy (*Schreiber, 2000*; *Vicente et al., 2011*)

and partial directed coherence (*Baccalá and Sameshima, 2001*). Each approach has its advantages and disadvantages [see (*Lindquist, 2008*; *Liu and Aviyente, 2012*) and the Discussion section below] in terms of the assumptions involved and the computational effort required. The fact that all methods currently used make assumptions the validity of which has not been fully tested, leaves room for introducing new measures of effective connectivity (*Lindquist, 2008*). This motivates the investigation of new measures of directed connectivity.

We have two goals in this paper. Our first goal is to advocate a new measure of data-driven effective brain connectivity by applying the novel concept of information flow rate to EEG signals. This goal is motivated by the need to define measures of connectivity that are based on fewer or more suitable model assumptions than commonly used methods (*Lindquist, 2008*). The information flow rate has several desirable properties (as summarized below and elaborated in the Discussion section) which give it unique advantages for connectivity analysis compared with standard methods. To the best of our knowledge, our study is the first to apply the information flow rate to neuroscience data. Our second goal is to analyze EEG resting-state data from a group of healthy adolescents using the information flow rate, in order to identify connectivity patterns in the adolescent brain. Only one prior study that focuses on this age group is available in the literature, and the connectivity analysis in that study is carried out in sensor space (*Marshall et al., 2014*).

The information flow rate was developed by Liang using the concept of information entropy and the theory of dynamical systems (*Liang, 2008*, *2013b*, *2014*, *2015*) and based on earlier work with Kleeman (*Liang and Kleeman, 2005*). While the the initial formulation of the information flow rate was derived for two-dimensional (bivariate) systems, *Liang* (*2016*, 2018) recently showed that the formulation is also valid for N-dimensional systems as well. The Liang-Kleeman coefficient can measure the transfer of information between time series at different locations and thus between different brain regions. Unlike empirical measures of causality, e.g., transfer entropy and Granger causality, the information flow rate is derived from general, first-principles equations for the time evolution of stochastic dynamical systems (*Liang, 2016*, *2018*). Owing to its definition, which involves only the time series and their temporal derivatives (or their finite-difference approximations for discretely sampled systems), the information flow rate has computational advantages over other entropy-based measures such as transfer entropy, that require the estimation of additional information (e.g., conditional probabilities) from the data. In addition, the information flow rate concept does not require stationarity (*Liang, 2015*) or a specific model structure, and can also be applied to deterministic nonlinear systems (*Liang, 2016*). These are important advantages, since the EEG signals exhibit non-stationary features evidenced in transitions between quasi-stationary periods and nonlinear dynamic behavior (*Blanco et al., 1995*; *Kaplan et al., 2005*; *Klonowski, 2009*).

Results

We set out to investigate patterns of resting-state effective connectivity in the brain of adolescent males, using source-reconstructed EEG signals (see Materials and methods). Our analysis of connectivity is based on the Liang-Kleeman information flow rate described in *Box 1*. The information flow rate measures the effect of a time series i, called *transmitter*, on a different time series j, called *receiver*. The indices i and j correspond to different brain source locations. In particular, we

109 use a normalized version of the information flow rate which is better suited for ranking pair-wise

110 information flow rates for an ensemble of N_s time series based on their relative impact on the

111 *receiver time series* (see Materials and methods for details). Herein $N_s = 15$ corresponds to the

112 numbers of source locations obtained by source-space reconstruction. The brief comment in **Box 2**

113 provides an intuitive understanding of causal relations in terms of the information flow rate.

170   To quantify effective brain connectivity, we use the *normalized information flow rate* $\tau_{i \to j}$ (defined

171 by **Equation 9** in Material and methods). The time series that we analyze involve the magnitudes of

172 fifteen *current dipole moments* per individual. These are obtained by means of source reconstruction

173 of scalp EEG signals as described in Materials and Methods. We focus on the *normalized inter-dipole*

174 *information flow rate* instead of the non-normalized $T_{i \to j}$, because we aim to capture interactions

175 between brain regions that significantly affect the *receiver* region (denoted by the index j). The

176 advantage of $\tau_{i \to j}$ is its ability to measure the *relative importance* of causal relations (**Liang, 2015**).

177   We use the second-neighbor differencing scheme (i.e., $k = 2$, see **Box 1**) to calculate the informa-

178 tion flow rates as suggested by **Liang** (**2014**). We further comment on this choice in Materials and

179 methods (section on the impact of differencing scheme).

180   Our analysis focuses on the *mean information flow rate* calculated over all the individuals in the

181 study cohort, but we also explore variations of connectivity between individuals.

Brain connectivity based on mean information flow rate

183 To study the information flow across brain regions we want to characterize connections that exhibit

184 significant levels of activity (as measured by the information flow rate) over all the individuals. We

185 do this using the *ensemble mean* of the normalized information flow rate $i \to j$ evaluated over the

186 cohort of $L = 32$ individuals:

$$\overline{\tau}_{i \to j} = \frac{1}{L} \sum_{l=1}^{L} \tau_{i \to j}^{(l)}, \ i \neq j = 1, \dots, N_s. \tag{5}$$

187   The top panel in **Figure 1** displays the patterns of the *mean information flow rate* $\overline{\tau}_{i \to j}$. The

188 variable $\overline{\tau}_{i \to j}$ for all values of *transmitter i* and *receiver j* source locations is represented by an $N_s \times N_s$

189 matrix that represents all possible (i.e., 210) connections between sources. The number of possible

190 connections is $N_s \times (N_s - 1)$ where $N_s = 15$ is the number of source dipoles. The value of a grid

191 cell (L1, L2), determined by the label L1 on the vertical axis and the label L2 on the horizontal axis,

192 represents information flow from dipole L1 to dipole L2. The matrix cells are colored according to

193 the value of $\overline{\tau}_{i \to j}$: the values increase as the color changes from blue to red. The cells along the

194 main diagonal are not colored, indicating that the information flow rate from $i \to j$ is only defined

195 if $i \neq j$. The color pattern (thus, also the matrix $\overline{\tau}_{i \to j}$) is *asymmetric* along the main diagonal. This

196 asymmetry reflects the directionality of the information flow rate, i.e., the fact that $\tau_{i \to j}$ is in general

197 different than $\tau_{j \to i}$.

198   A relevant question for interpreting the results is how many of the 210 connections (represented

199 by the off-diagonal matrix cells) shown in **Figure 1** are important. As we discuss in Material and

200 methods, it can be shown by *permutation testing* that the vast majority of the connections for all

201 the individuals are statistically significant even at the $p = 0.001$ level. However, very low values of

202 information flow rate, albeit statistically significant, imply that the relative impact of the *transmitter*

Manuscript submitted to eLife

Box 1. The Liang-Kleeman information flow rate

Let $\{p_i(t_n)\}_{n=1}^{N}$ denote a collection of N_s time series at different brain source locations indexed by $i = 1, \ldots, N_s$. Herein, the term "time series" implies EEG-derived series of current dipole moments.

The *Liang-Kleeman coefficient* $T_{i \to j}$ measures the rate of information flow from the time series i to the time series j (where $j \neq i$). $T_{i \to j}$ can be expressed in terms of *sample statistics* as follows (*Liang, 2014*)

$$T_{i \to j} = \frac{\widehat{r}_{i,j}}{1 - \widehat{r}_{i,j}^2} \left(\widehat{r}_{i,dj} - \widehat{r}_{i,j} \widehat{r}_{j,dj} \right), \text{ for } i, j = 1, \ldots, N_s, \ i \neq j. \tag{1}$$

In the above, the *linear (Pearson) sample correlation coefficient* between the time series p_i and p_j is defined by

$$\widehat{r}_{i,j} = \frac{\widehat{C}_{i,j}}{\widehat{\sigma}_i \widehat{\sigma}_j}, \text{ for } i, j = 1, \ldots, N_s, \ i \neq j, \tag{2}$$

where $\widehat{C}_{i,j}$ is the *sample cross-covariance* of the series p_i and p_j, and $\widehat{\sigma}_i = \sqrt{\widehat{C}_{i,i}}$ is the sample standard deviation of the series p_i ($i = 1, \ldots, N_s$). Both $\widehat{C}_{i,j}$ and $\widehat{r}_{i,j}$ (often used to measure functional connectivity) are non-directional and symmetric under the index interchange $i \leftrightarrows j$. The sample cross-covariance $\widehat{C}_{i,j}$ is defined by

$$\widehat{C}_{i,j} = \overline{p_i p_j} - \overline{p_i}\,\overline{p_j}, \text{ for } i, j = 1, \ldots, N_s,$$

where the "overline" denotes the sample time average, i.e., $\overline{p_i} = \frac{1}{N} \sum_{n=1}^{N} p_{i,n}$ and $\overline{p_i p_j} = \frac{1}{N} \sum_{n=1}^{N} p_{i,n} p_{j,n}$. If $i = j$ the above equation returns the variance of p_i, i.e., $\widehat{C}_{i,i} = \widehat{\sigma}_i^2$.

The *cross-correlation coefficients* $\widehat{r}_{i,dj}$, where $i, j = 1, \ldots, N_s$, in **Equation 1** involve the time series p_i and the *temporal derivative* $\mathrm{d}p_j/\mathrm{d}t$ of the time series p_j. These coefficients are expressed in terms of the respective covariances as follows

$$\widehat{r}_{i,dj} = \frac{\widehat{C}_{i,dj}}{\widehat{\sigma}_i \widehat{\sigma}_j}, \text{ for } i, j = 1, \ldots, N_s. \tag{3}$$

where $\widehat{C}_{i,dj}$ is the sample covariance of the time series p_i and the first derivative, $\mathrm{d}p_j/\mathrm{d}t$, of the series p_j. Due to the discrete nature of sampling, the first derivative $\mathrm{d}p_j/\mathrm{d}t$ is unknown *a priori*. Hence, a finite difference approximation based on the Euler forward scheme, with a time step equal to $k\Delta t$, is used, i.e.,

$$\frac{\mathrm{d}p_{j,n}}{\mathrm{d}t} = \frac{p_{j,n+k} - p_{j,n}}{k \, \Delta t}, \text{ for } j = 1, \ldots, N_s, \ n = 1, \ldots, N - k. \tag{4}$$

The differencing orders $k = 1$ and $k = 2$ are the two most common choices (*Liang, 2013a*) which we also consider herein.

Herein we refer to p_i as the *transmitter series* and to p_j as the *receiver series* with respect to $T_{i \to j}$. We adopt the term *transmitter* instead of "source" for the series that "sends" information in order to avoid confusion, since all the time series represent *current dipole moments* obtained from scalp EEG by means of *source reconstruction*.

Manuscript submitted to eLife

---

160 **Box 2. Causality and the Liang-Kleeman coefficient**

161 Consider two time series p_i and p_j, where $i, j = 1, \ldots, N_s$ and $j \neq i$. According to the Liang-

162 Kleeman formalism which is based on the notion of information entropy, the series p_j has a

163 causal effect on p_i if the rate of change of p_i depends on p_j. Conversely, p_i has a causal effect

164 on p_j if the rate of change of p_j depends on p_i. Hence, the following four possibilities arise:

165 1. Neither p_i influences p_j, nor p_j influences p_i : $T_{i \to j} = T_{j \to i} = 0$.

166 2. Only p_i influences p_j, but p_j does not influence p_i : $T_{i \to j} \neq 0$, $T_{j \to i} = 0$.

167 3. Only p_j influences p_i, but p_i does not p_i influence p_j : $T_{i \to j} = 0$, $T_{j \to i} \neq 0$.

168 4. Both p_i and p_j influence each other : $T_{i \to j} \neq 0$, $T_{j \to i} \neq 0$.

169 5. $T_{i \to i}$ does not have a physical meaning and is thus undefined.

---

203 series on the *receiver* is not neurologically important. On the other hand, there is no golden rule

204 for selecting a threshold value above which connections are considered important (*Cohen, 2014*).

205 Hereafter, we will consider that a connection $i \to j$ between two dipoles is *active in the ensemble*

206 *sense* if the magnitude of the normalized information flow rate $|\tau_{i \to j}|$ exceeds the arbitrary threshold

207 of $\tau_c = 0.05$. This means that the entropic rate of change at the *receiver* j due to its interaction

208 with the *transmitter* located at i is at least 5% of the total rate of entropy change at j. (We further

209 comment on the selection $\tau_c = 0.05$ in connection with *Figure 3* below.) The bottom panel of *Figure 1*

210 shows the mean information flow rate for the connections that are active in the ensemble sense.

211 The latter involve only connections such that $\overline{\tau}_{i \to j} \geq 0.05$. As evidenced in this plot, 92 out of the 210

212 inter-dipole pairs are connected on average, i.e., they exhibit $\overline{\tau}_{i \to j} \geq \tau_c$.

213 The top thirty (30) active connections, ranked on the basis of $\overline{\tau}_{i \to j}$, are listed in *Table 1* and

214 displayed by arrows on an axial view schematic in *Figure 2*. All thirty connections correspond to

215 positive values of $\overline{\tau}_{i \to j}$ in the interval between 0.116 (highest) and 0.072 (lowest). All of them have

216 values higher than the threshold $\tau_c = 0.05$. Evaluating the thirty top connections (cf. *Figure 2*), the

217 overall information flow pattern is predominantly left lateralized and consists of mostly short and

218 medium range bidirectional connections linking the frontal, central and temporal regions of the

219 brain. The possible neurological insights derived from *Table 1* and *Figure 2* are developed in the

220 Discussion section.

221 The last column of *Table 1* displays the *polarization* $P(\tau_{i \to j})$ of the information flow rate. This

222 ensemble measure is given by the average sign of $\tau_{i \to j}$ expressed as a percentage, i.e.,

$$P(\tau_{i \to j}) = \frac{100}{L} \sum_{l=1}^{L} \text{sgn}\left(\tau_{i \to j}^{(l)}\right), \qquad (6)$$

223 where $\text{sgn}(\cdot)$ is the sign function defined by $\text{sgn}(x) = 1$, if $x > 0$, $\text{sgn}(x) = -1$, if $x < 0$ and $\text{sgn}(x) = 0$, if

224 $x = 0$. The polarization is a number close to $\pm 100\%$ if the sign of the $\tau_{i \to j}$ is typically the same for

225 all the individuals (if all the signs are the same the polarization is 100%). In *Table 1* the polarization

226 varies between $\approx 88\%$ and 100% and is less than 100% only for eight connections. This means that

227 for the vast majority of connections, the variations between individuals affect the magnitude but
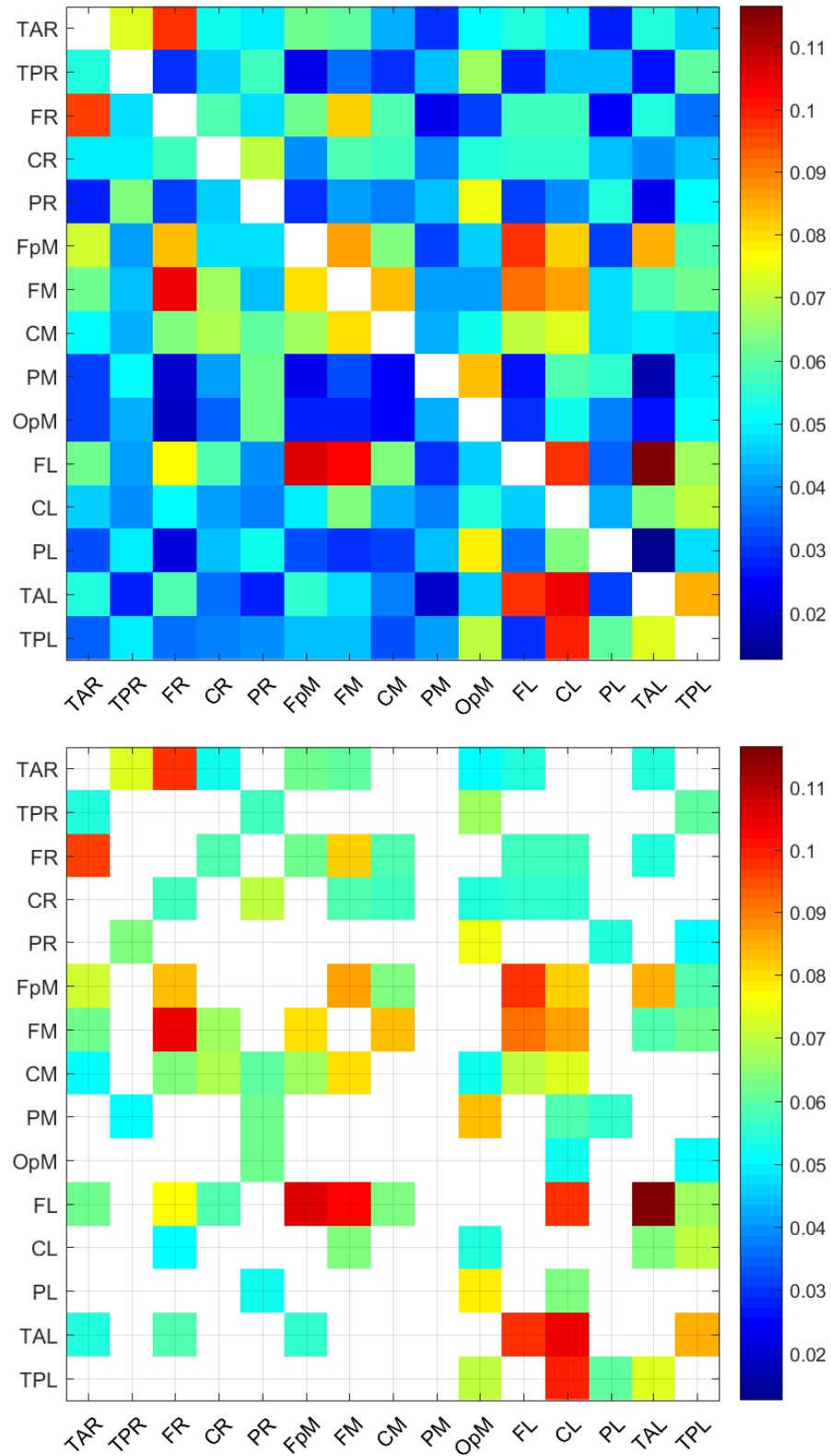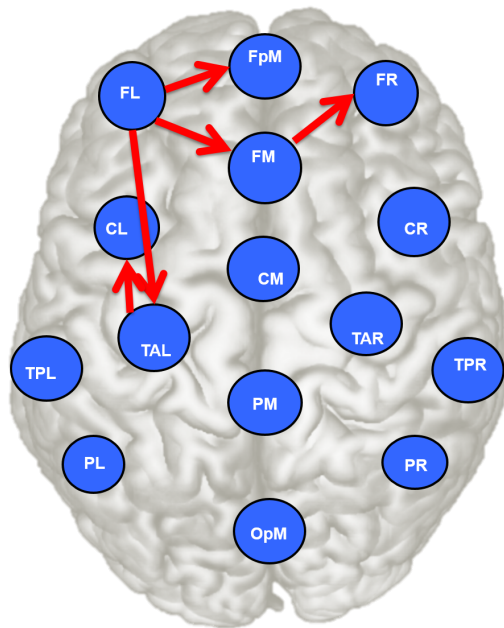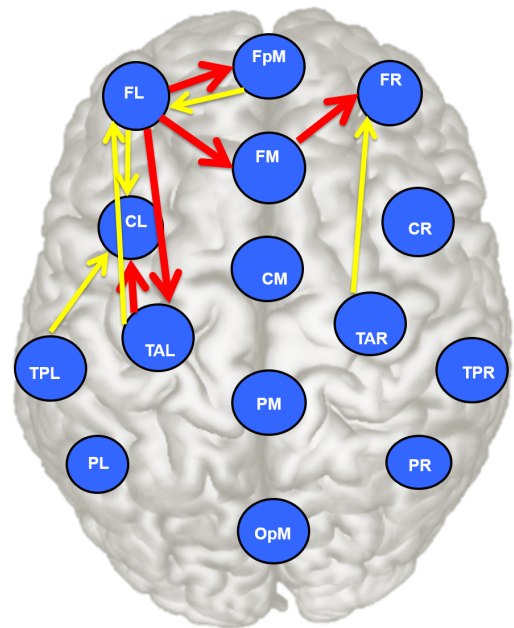
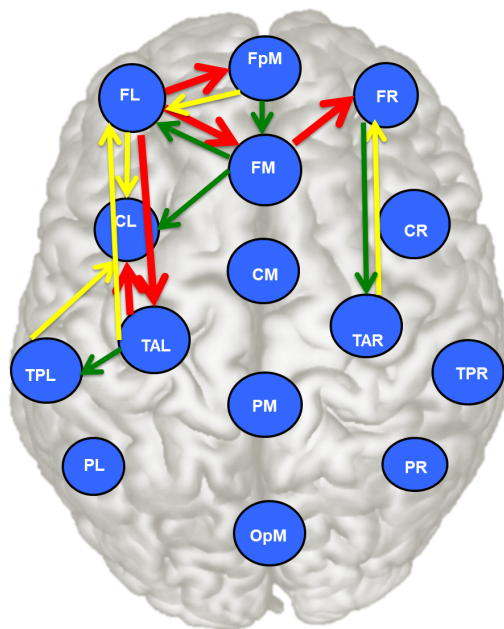228 not the sign of the normalized information flow rate.

Figure 1. Mean normalized information flow rates, $\overline{\tau}_{i \to j}$, calculated over all the individuals in the study cohort (top) and corresponding values for connections above the threshold $\tau_c = 0.05$ (bottom). There are 92 connections with $\overline{\tau}_{i \to j} \geq \tau_c$.
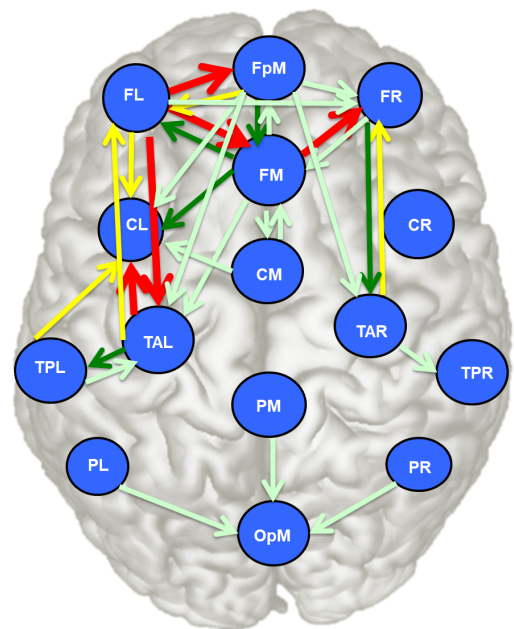
Manuscript submitted to eLife

(a) Top 5 connections

(b) Top 10 connections

(c) Top 15 connections

(d) Top 30 connections

Figure 2. Axial-view schematic showing the main pathways of information flow based on the mean normalized information flow rates shown in *Table 1*. The schematic shows the locations of the sources in BESA's 15 pre-defined regions (see Description of EEG data in Materials and methods. (a) Five most important connections shown in red arrows (color online). (b) Ten most important connections; connections ranked from six to ten are shown with yellow arrows. (c) Fifteen most important connections with those ranked from 11 to 15 shown with green arrows. (d) Thirty most important connections with those ranked from 15 to 30 shown in light green arrows (cf. *Table 1*).

Manuscript submitted to eLife

229   A different way to view the relation between the ensemble mean $\overline{\tau}_{i \to j}$ and the information flow

230   rates of individuals is by counting for how many individuals each connection is active. Hereafter, we

231   will consider that a connection $i \to j$ between two dipoles is *individually active* if the magnitude of the

232   normalized information flow rate $|\tau_{i \to j}|$ exceeds the threshold τ_c, which means that the percentage

233   of the total entropy rate of the *receiver* due to its interaction with the *transmitter* is at least 5%. We

234   assume that the threshold for individually active connections is the same as the threshold used for

235   the ensemble mean of the information flow rate. However, this is not necessary in general.

236   We define the *frequency of activity*, $n_{i \to j}(\tau_c)$, for the connection $i \to j$ as the number of individuals

237   in the study cohort for which the specific connection is active. Hence,

$$n_{i \to j}(\tau_c) = \sum_{l=1}^{L} \theta \left(|\tau_{i \to j}^{(l)}| - \tau_c \right), \tag{7}$$

238   where $\theta(\cdot)$ is the unit step function, i.e., $\theta(x) = 1$, for $x \geq 0$ and $\theta(x) = 0$ for $x < 0$. The frequency of

239   activity is evaluated over all the individuals and takes values integer $n_{i \to j}(\tau_c) \in \{0, 1, \dots, L\}$, where

240    $L = 32$ is the number of individuals in the cohort. The frequency of activity depends on τ_c, as higher

241   values of τ_c imply a smaller number of active connections.

242   In *Figure 3*, we explore the correlation between the ensemble mean $\overline{\tau}_{i \to j}$ and the number

243   of individually active connections $n_{i \to j}(\tau_c)$. The scatter plot shows an almost linear dependence

244   between the number of individually active connections and the respective value of $\overline{\tau}_{i \to j}$ for values

245   of $\overline{\tau}_{i \to j} \leq 0.07$ and appears to level off at higher values of $\overline{\tau}_{i \to j}$. At the same time, the scatter also

246   increases towards these higher values. We can also use this plot as a guide for selecting a suitable

247   threshold for ensemble-based connectivity analysis, since it reveals how the threshold imposed

248   on $\overline{\tau}_{i \to j}$ (shown as a vertical red line in *Figure 3*) affects the number of active connections, i.e., the

249   number of markers to the right of the vertical line at τ_c. However, note that the frequency of the

250   connections in individuals (i.e., the values on the vertical axis) will change if a different threshold

251   is used to estimate individual activity. Essentially, the plot would need to be redrawn for different

252   values of individual τ_c.

Information flow rate patterns per individual

254   To study the information flow across brain regions in individuals, we focus on the *individually active*

255   source dipole pairs. As stated above, these are dipole pairs with $\tau_{i \to j}$ whose magnitude (absolute

256   value) exceeds the threshold $\tau_c = 0.05$. We use the criterion $|\tau_{i \to j}| > \tau_c$ instead of $\tau_{i \to j} > \tau_c$ since there

257   are a few pairs (nine out of a total of 6720) with values of $\tau_{i \to j} < -0.05$.

258   For each of the 32 individuals in the study, we calculate 210 values of normalized inter-dipole

259   information flow rates $\tau_{i \to j}$. To calculate $\tau_{i \to j}$, we use all the time points in the EEG time series. The

260    $\tau_{i \to j}$ values over all individuals range from -0.0794 to 0.3568. The matrix of the $\tau_{i \to j}$ values *for each*

261   *individual* is depicted in *Figure 4-Figure 7*. Each plot corresponds to a single individual and shows

262   an $N_s \times N_s$ square grid that represents all the possible connections between sources. The value of

263   each grid cell in *Figure 1* is equal to the average (evaluated over all the individuals) of the values of

264   the respective grid cells in *Figure 4-Figure 7*.

265   These plots display the values of $\tau_{i \to j}$ for all source dipole pairs, regardless of whether the

266   connections are active with respect to the threshold τ_c or not. All the plots use a unified colormap

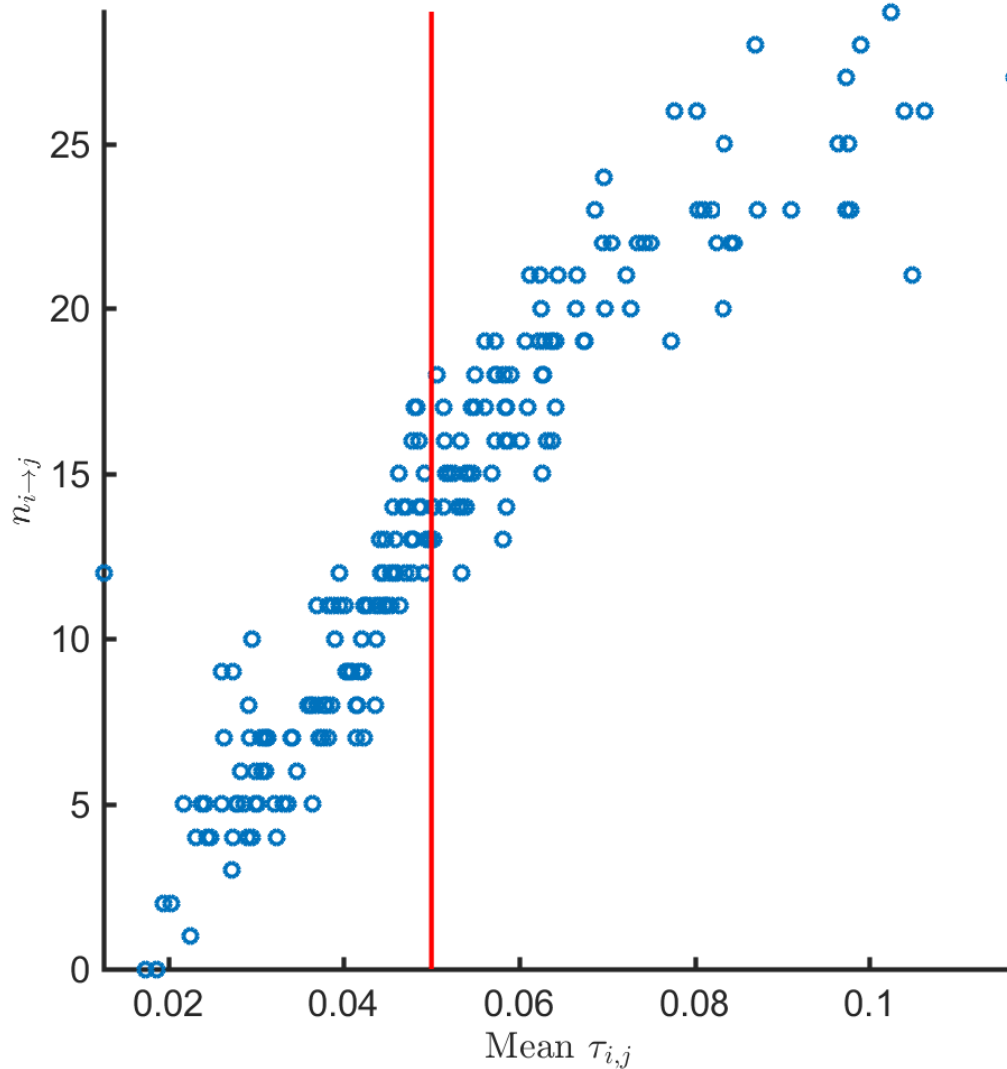**Figure 3.** Frequency $n_{i \to j}(\tau_c)$ of individually active connections (based on the individual threshold $\tau_c = 0.05$) plotted against the ensemble mean of normalized flow rate coefficient $\tau_{i \to j}$ for the connection *transmitter i → receiver j* for all $i \neq j = 1, \ldots, 15$. The plot comprises 210 points, each of which corresponds to a different $i \to j$ connection between two source dipoles. The frequency of activity $n_{i \to j}(\tau_c)$ is calculated over all $L = 32$ individuals in the cohort based on *Equation 7* and thus its upper bound is equal to L. The ensemble mean $\overline{\tau}_{i \to j}$ is calculated based on *Equation 5*. The vertical red line marks the threshold value $\tau_c = 0.05$. All the markers to the right of the vertical line correspond to connections $i \to j$ which are on average above the threshold.
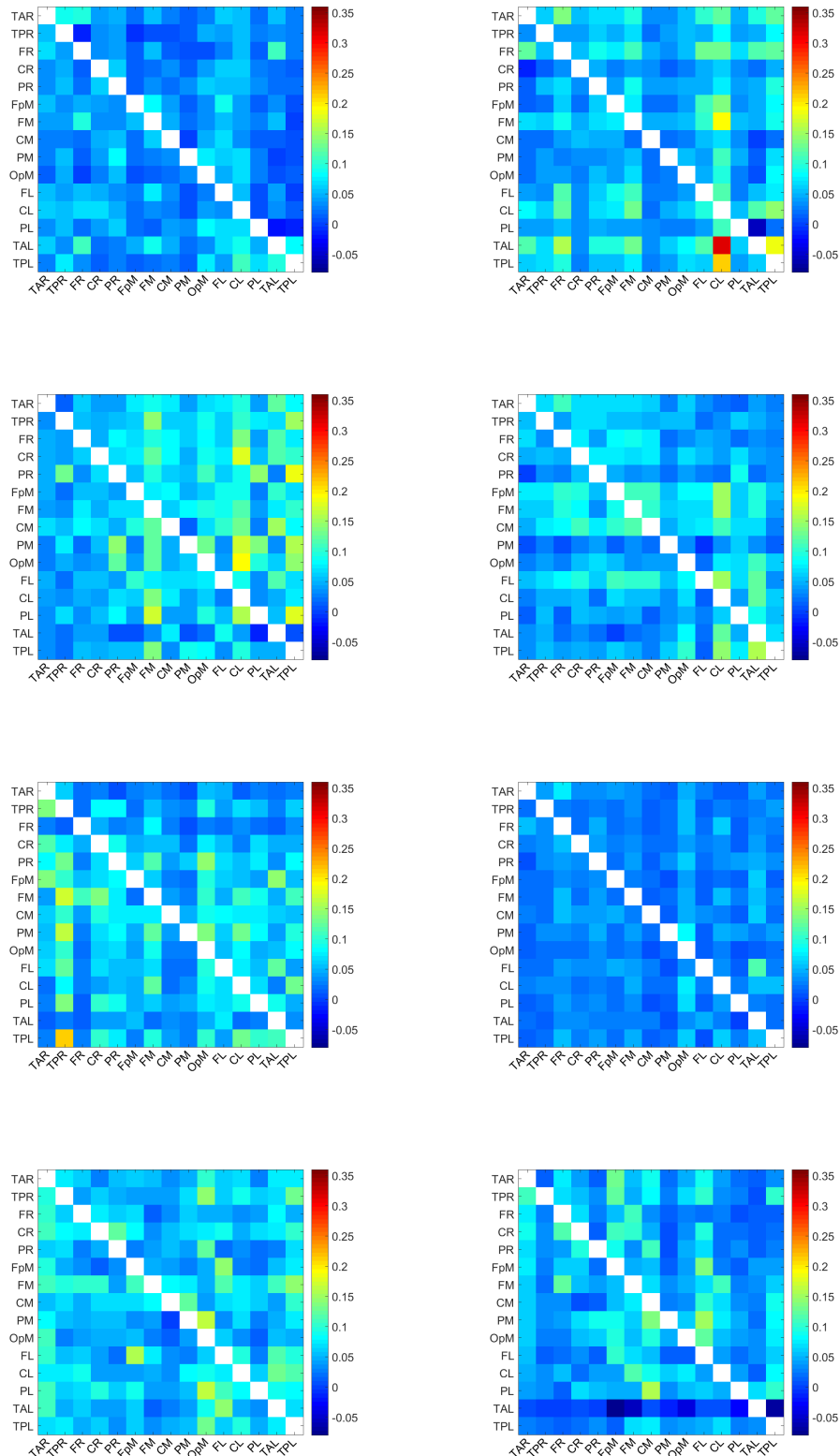
Figure 4. Map of $\tau_{i \to j}$ values for the individuals 1-8. A uniform color map is used based on the range of $\tau_{i \to j}$ values for all 32 individuals. The value of a grid cell (L1, L2), determined by the label L1 on the vertical axis and the label L2 on the horizontal axis, represents information flow from the dipole with label L1 to the dipole with label L2. The $\tau_{i \to j}$ values over all dipoles and individuals range from -0.08 to 0.36.
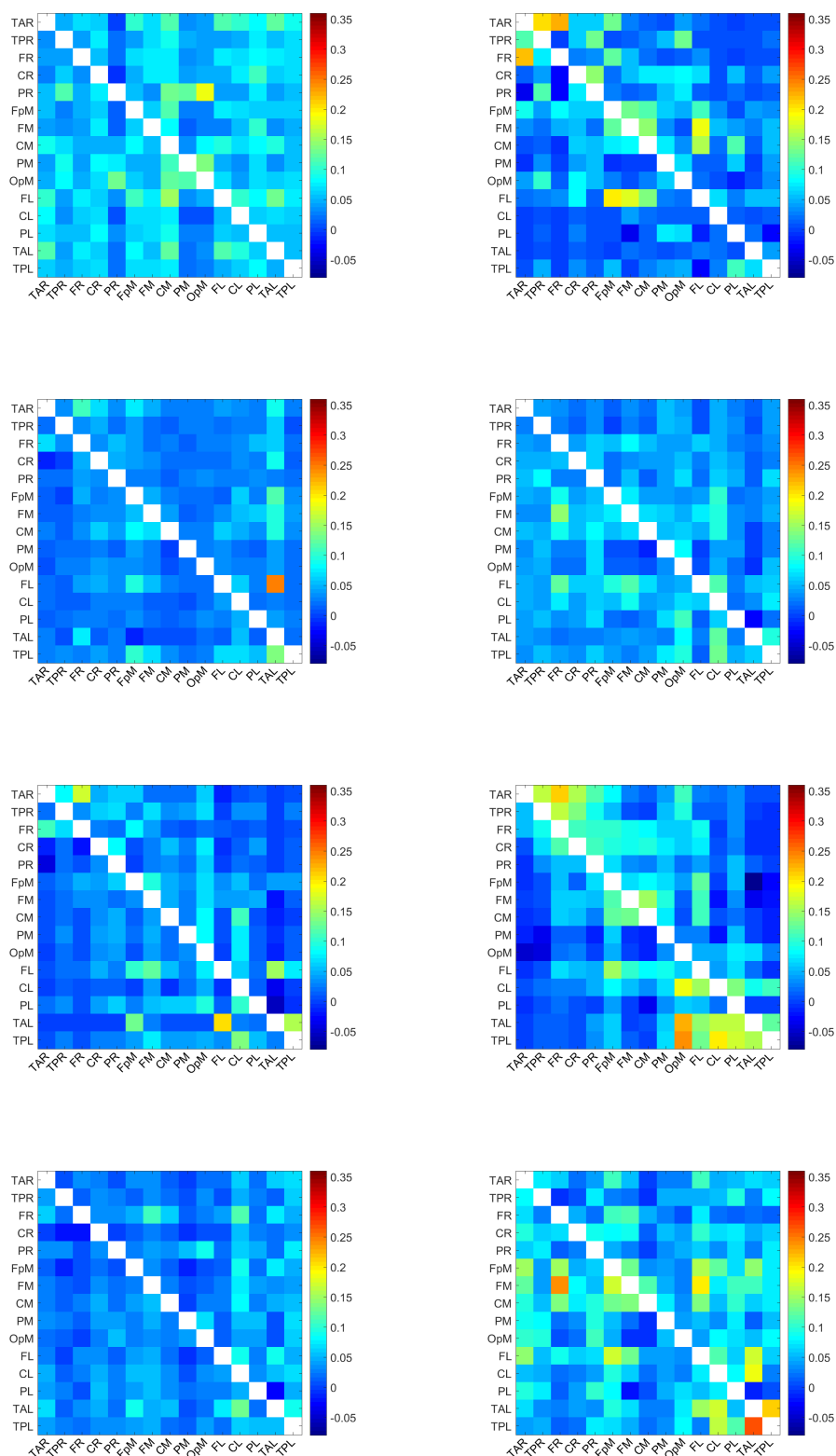
Figure 5. Map of $\tau_{i \to j}$ values for the individuals 9-16. A uniform color map is used based on the range of $\tau_{i \to j}$ values for all 32 individuals. The value of a grid cell (L1, L2), determined by the label L1 on the vertical axis and the label L2 on the horizontal axis, represents information flow from the dipole with label L1 to the dipole with label L2. The $\tau_{i \to j}$ values over all dipoles and individuals range from -0.08 to 0.36.
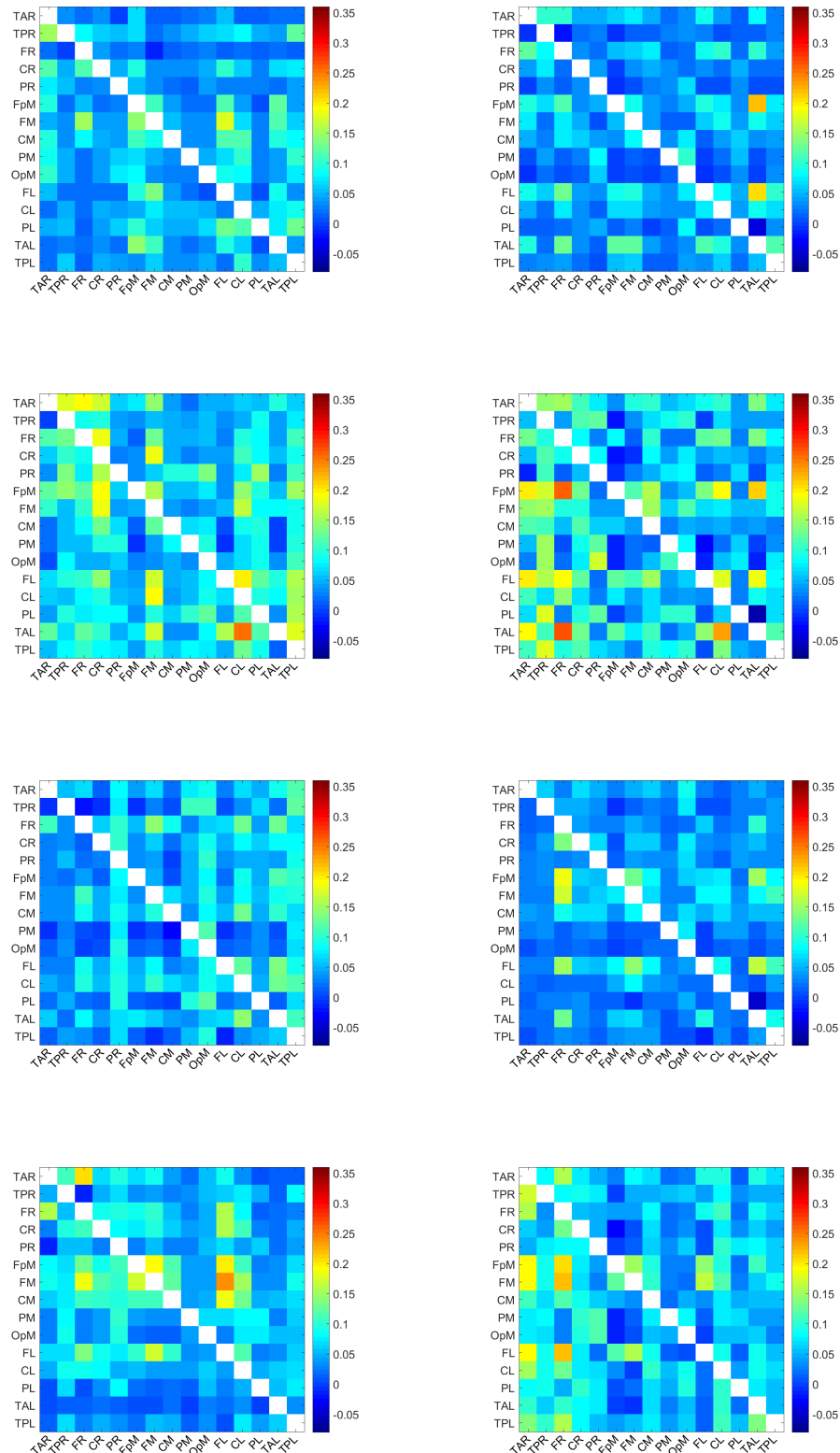
Figure 6. Map of $\tau_{i \to j}$ values for the individuals 17-24. A uniform color map is used based on the range of $\tau_{i \to j}$ values for all 32 individuals. The value of a grid cell (L1, L2), determined by the label L1 on the vertical axis and the label L2 on the horizontal axis, represents information flow from the dipole with label L1 to the dipole with label L2. The $\tau_{i \to j}$ values over all dipoles and individuals range from -0.08 to 0.36.

Figure 7. Map of $\tau_{i \to j}$ values for the individuals 25-32. A uniform color map is used based on the range of $\tau_{i \to j}$ values for all 32 individuals. The value of a grid cell (L1, L2), determined by the label L1 on the vertical axis and the label L2 on the horizontal axis, represents information flow from the dipole with label L1 to the dipole with label L2. The $\tau_{i \to j}$ values over all dipoles and individuals range from -0.08 to 0.36.
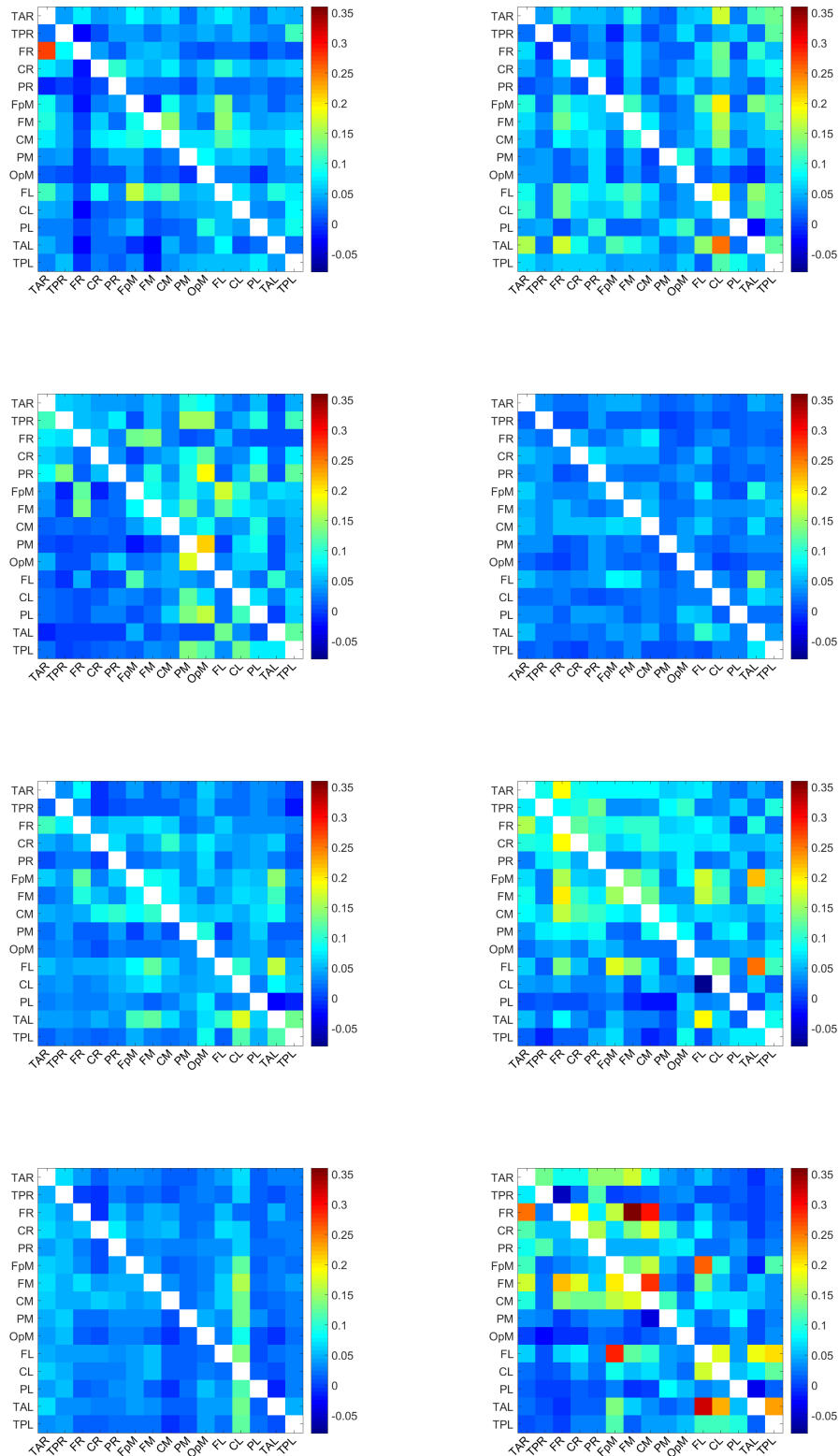
based on the full $\tau_{i \to j}$ range, i.e., $[-0.08, 0.36]$ calculated over all dipole pairs and individuals. We note that the $\tau_{i \to j}$ values are directional. For example, in the second plot (top right) of *Figure 4*, the cell labeled (TAL, CL) — near the bottom right of the grid — is colored red, which reflects a large value of $\tau_{i \to j}$, while the cell marked by (CL, TAL) — above the main diagonal of the grid — has a much lower $\tau_{i \to j}$. This indicates that the information flow from TAL has much higher impact on CL than the impact of CL on TAL.

The maximum $\tau_{i \to j}$ observed among individuals is ≈ 0.36. This is about three times higher than the highest ensemble mean $\overline{\tau}_{i \to j}$ which is equal to 0.116 (cf. *Table 1*). This difference reflects the variability of the information flow rate values between individuals.

Effective connectivity variations between individuals

To investigate the variability of the connectivity patterns between individuals, in *Figure 8* we plot the *frequency of activity*, $n_{i \to j}(\tau_c)$, defined in *Equation 7*, for all $i \neq j = 1, \dots, 15$ and for $\tau_c = 0.05$. The main features evidenced in this plot are as follows:

1. Almost all the possible (208 out of 210) *transmitter $i \to$ receiver j* inter-dipole connections are active in at least one individual.

2. Of the $210 \times 32 = 6720$ pairs of inter-dipole connections that are available *in total* in the cohort of 32 individuals, only 2821 connections, or about 42% of the total number, are individually active (i.e., their magnitude is not less than $\tau_c = 0.05$). This means that more than half of the current source dipole pairs in the study cohort are not strongly connected. In these pairs, the *transmitter* dipole does not strongly affect the *receiver* dipole.

3. In light of (1) and (2), we conclude that the active connections vary to some extent between individuals. For example, if the same set of about 42% connections were active for all (32) the individuals in the cohort, approximately 88 (i.e., 42% of 210) dipole pairs would be active. However, more than twice as many (i.e., 208) show active connections. In particular, 142 inter-dipole connections are active in ten or more individuals, forty inter-dipole connections (i.e., about 20% of the total connections) are active in twenty or more individuals, and twelve are active in more than 25 individuals.

The connectivity map in *Figure 8* exhibits a denser network of connections than the respective map in the bottom plot of *Figure 1*. The former shows the number of individuals for which a particular inter-dipole connection is individually active. Hence, it includes connections that are active in single individuals. On the other hand, the bottom plot in *Figure 1* displays the number of connections that are *active on average*, which is understandably smaller given the inter-subject variability. It is noteworthy that the five connections with the highest mean $\tau_{i \to j}$, i.e., FL→TAL, FL→FpM, TAL→CL, FM→FR, FL→FM (cf. Figs. *Figure 1* and *Figure 2*, and *Table 1*), have relatively high frequencies of activity $n_{i \to j}(0.05) = 27, 26, 21, 26, 29$ respectively. In other words, these connections are active in most of the individuals (cf. *Figure 8*).

Discussion

In this section we first discuss methodological aspects that are related to the information flow rate as well as its relation and differences with other connectivity measures. Then, we analyze the
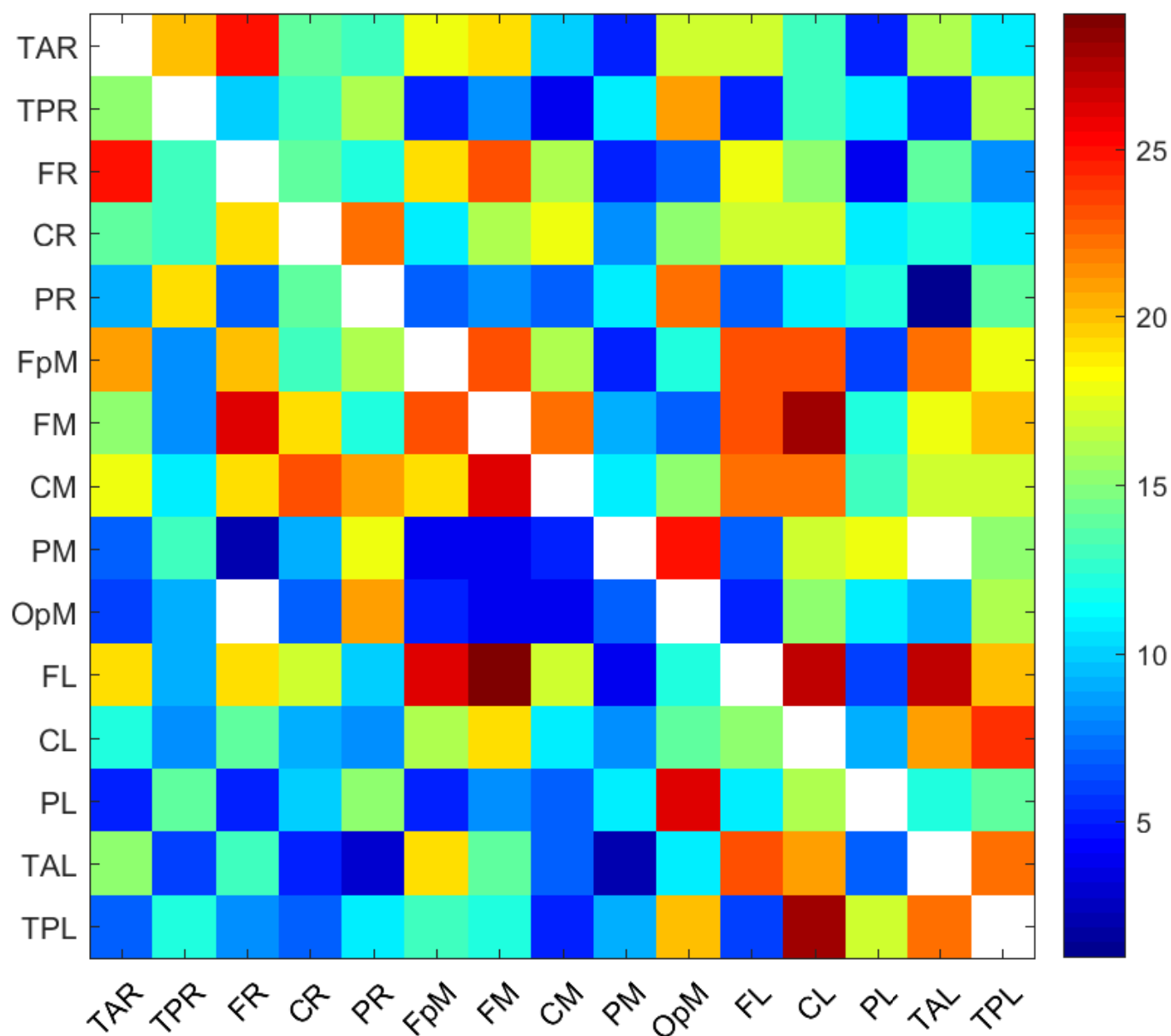
Figure 8. Frequency, $n_{i \to j}(\tau_c)$, of active connections (i.e., source current dipole pairs with $\tau_{i \to j}$ exceeding in magnitude the threshold value $\tau_c = 0.05$) calculated over all the individuals in the study. The value at each cell corresponds to the number of individuals for whom the specific connection is active. The white areas consist of cells with zero $n_{i \to j}(\tau_c)$, i.e., inactive connections. The diagonal cells are also white, since connections between the same *transmitter* and *receiver* are not meaningful.

results that we obtained in this study in the context of the existing literature results on effective brain connectivity, focusing on the resting state of the adolescent brain.

Brain connectivity measures and information flow

Functional measures of connectivity estimate non-directional relations and thus lead to undirected brain networks that fail to capture how one brain region influences another. However, such measures are still in common use (*Mill et al., 2017*). The simplest measure of functional connectivity is Pearson's linear correlation coefficient (*Cohen, 2014*). Pearson's coefficient fails to satisfactorily capture nonlinear dependence. Mutual information is a measure of functional connectivity that is based on information theory and can detect both linear and nonlinear relations (*Salvador et al., 2010*). Its calculation, however, requires the univariate probability distribution of each individual EEG time series, as well as the bivariate (joint) distribution for each pair of time series. Since long time series are required to estimate the bivariate distribution, the application of mutual information can be computationally intensive. Moreover, the method is sensitive to the number of bins used to estimate the probability histograms, and it fails to distinguish between nonlinear and linear, or positive and negative relations (*Cohen, 2014*).

On the other hand, measures of effective connectivity are directional variables which can distinguish the direction of information flow between brain regions. Measures of effective connectivity, such as *Granger causality* (*Kamiński et al., 2001*; *Hesse et al., 2003*; *Bressler and Seth, 2011*; *Seth et al., 2015*) and *transfer entropy* (*Schreiber, 2000*; *Liu and Aviyente, 2012*; *Salvador et al., 2010*; *Shovon et al., 2014*; *Hillebrand et al., 2016*), have been applied to EEG data to identify patterns of information flow in the functional brain networks during cognitive activity. Recently, *Muthuraman et al.* (*2015*) applied *renormalized partial directed coherence*, a measure based on the principle of Granger causality, to the combination of EEG and magnetoencephalography (MEG) signals to identify the direction of information flow between two signals and ultimately characterize the functional and effective connectivity in resting-state brain connectivity patterns. Thus, effective connectivity measures offer insights into the dynamics of the neuronal clusters that underpin cognitive function. Graphical models provide an intuitive tool for analyzing and visualizing associations and causal relationships and for modelling functional connectivity between brain regions (*Li and Wang, 2009*).

Granger causality analysis is based on the assumptions that (1) the time series are stationary, (2) interaction between the series can be described by means of a linear relation (typically a multivariate autoregressive model), (3) a specific model order can be defined, which determines how far in the past the coupling between two series extends, and (4) the innovation process of the linear model is described by Gaussian white noise (*Seth, 2007*; *Liu and Aviyente, 2012*; *Cohen, 2014*). This "plain vanilla" variety of Granger causality fails to detect nonlinear causal links (*Liu and Aviyente, 2012*; *Lin et al., 2017*). In such cases, nonlinear extensions of Granger causality are necessary (*Chen et al., 2004*; *Marinazzo et al., 2011*). However, such approaches are not yet conclusive since the selection of the degree of model nonlinearity and overfitting remain open issues (*Marinazzo et al., 2011*).

Transfer entropy is an extension of the concept of mutual information. It is based on the notion of relative entropy (also known as Kullback–Leibler divergence) and measures the difference between two probability distributions. For linear autoregressive systems driven by Gaussian white

Manuscript submitted to eLife

346 noise, Granger causality has been shown to be equivalent to transfer entropy (*Barnett et al., 2009*;

347 *Liu and Aviyente, 2012*). Hence, the latter can be viewed as an extension of the former that can

348 handle the dependence of non-Gaussian time series. Comparisons between Granger causality and

349 transfer entropy are given in (*Bressler and Seth, 2011*; *Liu and Aviyente, 2012*). As stated above,

350 Granger causality requires the specification of the order of the autoregressive processes involved.

351 This model order, however, may depend on a number of variables including the conditions, the

352 tasks executed (for task-oriented studies), and the EEG time series segments analyzed (*Cohen, 2014*).

353 Transfer entropy makes fewer assumptions about the data than the standard Granger causality

354 approach (*Vicente et al., 2011*). There are, nonetheless, challenges related to the calculation of

355 transfer entropy, e.g., estimation by state-space partitioning, as discussed by *Bressler and Seth*

356 (*2011*) and *Liang* (*2014*).

357   Entropy and information content are key concepts in the definition of functional and effective

358 brain connectivity measures (*Cohen, 2014*). In the thermodynamic sense, entropy is associated

359 with disorder: a higher temperature implies higher entropy. In classical (as opposed to quantum

360 mechanical) thermodynamics, the entropy S is calculated by means of the Gibbs formula $S =$

361 $-k_B \sum_i p_i \ln p_i$, where the summation is over the probabilities p_i of the system's microstates (the

362 index i should not to be confused with the location index of current source dipoles) and k_B is

363 Boltzmann's constant. In information theory, the entropy of a system with N states is defined in

364 terms of Shannon's formula $H = -\sum_{i=1}^{N} p_i \ln p_i$, where p_i, $i = 1, \dots, N$ is the probability of the state

365 indexed by i. If the natural logarithm is used in the definition (as was done above), Shannon entropy

366 is measured in terms of *natural information units (nats).*

367   The Shannon entropy quantifies the unpredictability (uncertainty) of a stochastic system. High

368 entropy implies that the result of a measurement is not only *a priori* unpredictable, but that the

369 measurement itself provides new information which improves our knowledge of the system. On

370 the other hand, low entropy means that the extant knowledge of the system allows us to predict

371 quite well the outcome of the measurement and consequently, the measurement does not contain

372 significant new information. Hence, higher entropy implies a higher level of unpredictability, while

373 lower entropy implies that efficient, "compressed" representations are possible (i.e., a parameter

374 set of lower dimensionality can be used to represent the system). In complex systems, there

375 are interactions between different components. We can intuitively view information flow from

376 component X to component Y as the amount of the uncertainty of Y that is resolved by the past

377 states of X. If the past states of the component X do not affect the current state of Y, there is

378 no information flow from X to Y (*Bossomaier et al., 2016*). On the other hand, the past states

379 of X may reduce or improve the predictability of Y, thus implying information flow from X to Y.

380 Currently used measures of functional and effective brain connectivity are based on the concept of

381 the absolute Shannon entropy. The concept of Shannon entropy has been generalized to dynamical

382 systems that are not necessarily stochastic, by means of the Kolmogorov-Sinai entropy (*Gutzwiller,*

383 *1990*) which quantifies the unpredictability of future states of the system.

384   The *Liang-Kleeman* information flow rate is a recently developed measure which is also based

385 on the concept of Shannon entropy (*Liang, 2008*, *2013b*,a, *2014*). However, the information flow

386 formalism can be derived using either absolute or relative entropy. In two dimensions (i.e., for a

system of two time series) this was shown by *Liang* (*2013b*, 2014). *Relative entropy* (Kullback–Leibler divergence) measures how much information is added to a given system with respect to the information contained in the initial probability distribution. Recently, *Liang* (*2018*) has shown that the relative entropy formulation of the information flow rate is also valid for stochastic dynamical systems with $N > 2$ dimensions (i.e., systems involving N potentially coupled time series, where N is an arbitrary integer value).

The information flow rate formulation is based on the theory of dynamical systems, in contrast with transfer entropy which is a statistically motivated measure of information transfer. The information flow rate aims to address the computational shortcomings of transfer entropy (requirement for long time series, computational complexity, estimation of bivariate probability distribution) as well as spurious causal associations (*Liang, 2016*). The information flow rate provides an easy-to-compute *directional (asymmetric)* measure of dependence between pairs of time series that can be evaluated from a single realization of each series and does not require the estimation of transition probabilities. Unlike Granger causality, the information flow rate concept does not require a specific model structure, Gaussian statistics, or stationarity (*Liang, 2015*) and can also be applied to deterministic nonlinear systems (*Liang, 2016*). These could be important advantages of information flow, since the EEG signals exhibit non-stationary features evidenced in transitions between quasi-stationary periods and nonlinear dynamic behavior (*Blanco et al., 1995*; *Kaplan et al., 2005*; *Klonowski, 2009*), while the correct model structure is never known *a priori*. However, further study is needed to compare in detail the performance of the information flow rate against the standard methods of assessing brain connectivity.

Finally, we draw attention to an ongoing discussion in the literature regarding the very definition of *effective connectivity*, e.g. (*Lindquist, 2008*). Friston argues that effective connectivity should be based on dynamic models, such as the Dynamic Causal Models (DCMs) (*Friston, 2011*). Model-based connectivity methods assume a well-defined biophysical model of neuronal dynamics (*Sakkalis, 2011*). Friston also opines that data-driven models, such as Granger causality, provide functional connectivity measures, a view that is echoed by *Bastos and Schoffelen* (*2015*). On the other hand, several other publications referenced in this paper, including the reviews (*Sakkalis, 2011*; *Bastos and Schoffelen, 2015*), refer to causality-based methods, including data-driven methods such as Granger causality and transfer entropy, as effective connectivity measures. We follow the latter viewpoint, according to which the information flow rate is an effective connectivity measure.

Comparison of brain connectivity results with literature

In recent years, a number of advances facilitating the study of functional connectivity of the brain have thoroughly transformed our understanding of the activity present in the brain in absence of "any imposed stimuli, task performance or other behaviourally salient events" [for a review, see (*Snyder and Raichle, 2012*)]. This "resting state" of the brain is characterized by spontaneous, coherent fluctuations of blood-oxygen-level-dependent (BOLD) as well as electromagnetic signals from functionally distinct brain regions. fMRI studies were the first to show that subsets of these regions tend to act in concert, giving rise to functionally relevant "resting-state" brain networks (*Raichle et al., 2001*; *Greicius et al., 2009*) that provide a basis for information processing and coordinated activity.

427 More recently, *Yuan et al.* (*2016*) and *Liu et al.* (*2017*) have found that functional resting-state
428 networks can also be extracted from source-space EEG data, and *Hillebrand et al.* (*2016*) have done
429 the same using MEG data. The most commonly reported resting-state functional networks observed
430 in children (*Muetzel et al., 2016*), adolescents (*Borich et al., 2015*) and adults (*Yuan et al., 2016*;
431 *Liu et al., 2017*) (and references therein) include the visual, the fronto-parietal, the sensory motor
432 and the default mode network (DMN). These studies also highlight that the above resting-state
433 functional networks are not independent, and that there is a high degree of interconnections
434 between them. To date, however, very few studies have investigated the information flow between
435 the different networks.

436 To our knowledge, there are only three studies that have investigated the source space informa-
437 tion flow pathways in adults (age: over 20 years) during eyes closed resting state, and considered
438 the relationship between these pathways and the underlying functional networks: (1) *Michels*
439 *et al.* (*2013*) study EEG data using the partial directed coherence (PDC) measure, which is based on
440 Granger causality, to quantify effective connectivity; (2) *Muthuraman et al.* (*2015*) analyze both EEG
441 and MEG data, also by means of the partial directed coherence (PDC) measure; and (3) *Hillebrand*
442 *et al.* (*2016*) study MEG recordings using directed phase transfer entropy (dPTE) to assess effective
443 connectivity. All three studies find that the dominant pattern in adults is a posterior to anterior
444 flow, originating in the regions associated with the primary visual cortex and the posterior DMN,
445 and flowing to the frontal regions. *Michels et al.* (*2013*) and *Muthuraman et al.* (*2015*) observe only
446 one-way connectivity between the brain regions. However, *Hillebrand et al.* (*2016*) find that the
447 dominant patterns are complemented by weaker anterior to posterior connections which make the
448 flow bidirectional at finer connection strength resolution.

449 Only *Michels et al.* (*2013*) have investigated source-space resting-state directed connectivity in
450 children (mean age: 10 years). They find that the dominant flow pattern is opposite to that observed
451 in the adults, with activation originating in the anterior (i.e. pre-frontal) regions and terminating in
452 the posterior (parietal/occipital) regions. One possible explanation is that the anterior to posterior
453 flow in children indicates modulation of lower-order sensory-motor information from frontal
454 regions (*Emberson et al., 2015*; *Taylor and Khan, 2000*). Admittedly, there are obvious gaps in our
455 understanding of the resting-state dynamics over the course of development. More studies of
456 the resting-state dynamics in children, as well as detailed comparisons with other populations at
457 different stages of development are needed to fully contextualize these findings.

458 The present study provides the first critical step towards understanding information flow in
459 the brain during a key transition stage between childhood and adulthood. We have analyzed
460 resting-state EEG data from an intermediate population, a cohort of adolescents (mean age: 16
461 years). Using the Liang-Kleeman information flow rate as a measure of effective brain connectivity,
462 we find that of the 30 *active* connections in adolescent brains (based on the ensemble means of the
463 normalized information flow rate), the five strongest (cf. red arrows in *Figure 2*a) mostly originate
464 in the left frontal region of the brain and flow to left temporal and mid-frontal regions. Including
465 the next ten connections (cf. yellow and dark green arrows in Figs. *Figure 2*b and *Figure 2*c) extends
466 the active areas of the brain beyond the frontal region to encompass adjacent posterior regions
467 (i.e., central and temporal), with the information flow pattern becoming largely bidirectional but

still strongly left lateralized. The final fifteen connections (cf. light green arrows in *Figure 2*d) are characterized by information flows between mainly the left and mid anterior regions. They also show some slightly lower level activity on the right side of the brain, an indication of inter-hemispheric flow between the left and right frontal regions, and the emergence of connections in the posterior regions (i.e. parietal to occipital). Overall, the information flow pattern suggested by the thirty connections is highly left lateralized and comprises mostly short and medium range bidirectional connections that link the frontal, central and temporal regions of the brain.

The above results are reminiscent of the basic directed connectivity pattern observed by *Michels et al.* (*2013*) in young children but with one important difference. In early adolescence, the pattern of information flow manifests an additional layer of complexity indicated by bidirectional communication between brain regions that *Hillebrand et al.* (*2016*) observe in the adults and which they interpret as feedback loops. In effect, the pattern that we observe in our cohort suggests a progression towards maturation of the adolescent brain.

Similarly, the lateralization of the information flow we observe is also a reflection of an earlier developmental stage. *Agcaoglu et al.* (*2015*) studied individuals ranging from 12 to 71 years and observed that the resting-state networks of young individuals are highly lateralized, with the default mode network, attention and frontal networks being strongly left lateralized. With age, however, this lateralization decreases and the network becomes more symmetric. In fact, the degree of interaction between networks, the order in which the networks are activated, the organization and the strength of the interactions within individual networks (including the extent to which they are lateralized), all change over development (*Muetzel et al., 2016*).

The fact that both functional and effective connectivity changes as the brain matures is not entirely surprising. It is well known that the brain undergoes considerable structural changes during the transition from puberty to adulthood (*Shaw et al., 2008*) as manifested by significant increase (decrease) in the volume of white (grey) matter (*Gogtay et al., 2004*; *Paus, 2005*; *Toga et al., 2006*; *Lebel and Beaulieu, 2011*). For example, *Lebel and Beaulieu* (*2011*) have shown that while the maturation of the projection fibers linking the primary sensorimotor cortical regions with lower-order subcortical sensory areas and the commissural fibers connecting the two hemispheres of the brain is mostly complete by late adolescence, the maturation of the association tracts, particularly the superior longitudinal and fronto-occipital fasciculi that connect the occipital and the frontal regions of the brain, continues well into the twenties. Functionally, these long association fibers are correlated with increasing long-range EEG coherence and synchronization (*Miskovic et al., 2015*).

Finally, we have also identified significant variability of effective connectivity between individuals based on the patterns of information flow rate between brain regions. We have presented and discussed graphical tools for visualizing and characterizing variability between individuals including dipole-dipole connectivity plots that account for all the individuals in the cohort, e.g., *Figure 8*. The variability of the brain's resting-state functional and effective connectivity across individuals and over time are topics of considerable interest within both research and clinical settings. *Hutchison et al.* (*2013*) and *Hirayama et al.* (*2016*) (see also references therein) argue that the variability of the connectivity matrix between individuals is not due to noise but is associated with individual variances in mental/vigilance states and cognitive function. They also note that there are reports

of the temporal dynamics of the connectivity matrix being affected by brain health, which raises the exciting possibility that, in the future, the associated features could serve as disease/injury biomarkers. The significant advantages of the new data-driven measure of effective brain connectivity discussed in this paper (i.e., ease of calculation, sensitivity to both linear and nonlinear relations, independence from a specific model structure and the stationarity assumptions), make it especially well suited for exploring these exciting new directions.

Materials and Methods

In this section we briefly describe the EEG dataset. We then present the Liang-Kleeman directional information flow rate that will be used for the analysis of resting-state EEG brain connectivity. We also discuss how to numerically calculate and evaluate the statistical significance of the information flow rate obtained from the EEG data.

Ethics Statement

This study was approved by the University of British Columbia Clinical Research Ethics Board (Approval number: H17-02973). The adolescents' parents gave written informed consent for their children's participation under the approval of the ethics committee of the University of British Columbia and in accordance with the Helsinki declaration. All participants provided assent.

Participants

Thirty-two (32) right-handed male adolescents (mean age: 15.8 yrs; SD: ± 1.3) participated in this study. Exclusion criteria for all individuals included focal neurologic deficits, pathology and/or those on prescription medications for neurological or psychiatric conditions. Parents signed an informed consent form that was approved by the University of British Columbia and all participants provided assent.

Description of EEG data

Between 5–8 minutes of resting-state EEG data were collected while participants had their eyes closed, using a 64-channel Hydrogel Geodesic SensorNet (EGI, Eugene, OR) connected to a Net Amps 300 amplifier (*Virji-Babul et al., 2014*). The sensor-space signals were referenced to the vertex (Cz) and recorded at a sampling rate of $f_s = 250$ Hz. The scalp electrode impedance values were typically less than 50 $k\Omega$. To eliminate artifacts associated with attaching (removing) the cap, 750 data points were removed from the beginning (end) of each time series. (This corresponds to removing data with a total duration of 6s.) The EEG time series were then filtered using a band-pass filter (4–50 Hz) and a notch filter (60 Hz), as described in (*Porter et al., 2017*) [see also (*Rotem-Kohavi et al., 2014*, *2017*)], to remove signal drift and line noise. In addition, Independent Component Analysis (ICA) was used to identify, decompose and remove eye blinks. Finally, the data were visually inspected and epochs with motion as well as additional ocular artifacts were excluded, as were channels with excessive noise. Each of the resulting EEG series used in this study involves between 67,845 and 114,304 time points.

Next, we used the Brain Electrical Analysis (BESA) Version 6.3 software[1] (MEGIS Software GmbH,

---

[1] http://www.besa.de

Manuscript submitted to eLife

546 Gräfelfing, Germany) to map the cleaned sensor-space data to source waveforms. The voltages from
547 the available sensor channels were first interpolated to voltages at 81 predefined scalp locations
548 that comprise BESA's Standard-81 10-10 Virtual Montage (*BESA Wiki, 2018*) and re-referenced to
549 the average reference by subtracting the mean voltage of the full set of 81 virtual scalp electrodes.
550 BESA uses spherical splines interpolation to perform this mapping (*Perrin et al., 1989*; *Scherg*
551 *et al., 2002*). The interpolation offers a consistent way of dealing with occasional bad channels
552 while maintaining a common montage across all the individuals. Thereafter, we use the BESA
553 montage method (*Scherg et al., 2002*) to compute source waveforms. Since resting-state activity
554 is not localized, we used the BR_Brain Regions montage which is derived from 15 pre-defined
555 regional sources that are symmetrically distributed over the entire brain. The respective brain
556 regions involved in this montage are listed in Table 2 and shown in *Figure 2*. BESA uses a linear
557 inverse operator of the lead field matrix, which accounts for the topography of the sources included
558 in the BR_Brain Regions montage, to calculate the source waveforms (*Scherg et al., 2002*). The
559 composite source activity in each brain region is represented by a single regional source. Each
560 source is modeled as a current dipole whose moment is specified in terms of a *local* orthogonal
561 coordinate system with basis vectors commonly labelled as radial (r), horizontal (h), and vertical
562 (v). Thus, the source waveforms represent time series of the fifteen current dipoles. Finally, the
563 resulting data were exported to MATLAB for the analysis described below.

564 **Definition of inter-dipole information flow rate**

565 In the following, $p_i^{(l)}(t_n)$ will denote the time series quantifying the time-varying strength (magnitude)
566 of the current dipole moment at the source location i (where $i = 1, \dots, N_s = 15$) for the individual
567 indexed by l (where $l = 1, \dots, L = 32$), at time $t_n = n \Delta t$, where $n = 1, \dots, N$ is the time index and
568 $\Delta t = 4$ms is the *time step*. In terms of the dipole moment components $\left(r_i^{(l)}(t_n), h_i^{(l)}(t_n), v_i^{(l)}(t_n) \right)$ in the
569 local (r, v, h) system, the magnitude of the dipole moment is given by

$$p_i^{(l)}(t_n) \equiv \sqrt{ \left[r_i^{(l)}(t_n) \right]^2 + \left[h_i^{(l)}(t_n) \right]^2 + \left[v_i^{(l)}(t_n) \right]^2 },$$

570 For completeness, we note that in general both the strength and the orientation of the current
571 dipoles vary with time; however, in the present study, we track only their strength. In addition, we
572 drop the individual index l if there is no risk of confusion. For short, we will also write $p_{i,n} = p_i(t_n)$.

573 Unlike the Pearson correlation coefficient which satisfies $-1 \leq \hat{r}_{i,j} \leq 1$ due to Schwartz's inequality,
574 the magnitude of the coefficient $\hat{r}_{i,dj}$ is not constrained to be less than one. This is due to the
575 normalization of $\hat{r}_{i,dj}$ by the standard deviation of p_j instead of the standard deviation of the
576 temporal derivative $\mathrm{d}p_j/\mathrm{d}t$ (cf. *Equation 3*).

577 Based on the discussion of Shannon entropy (cf. Discussion section), a positive (negative) rate
578 of information flow from $i \rightarrow j$ ($T_{i \rightarrow j}$) indicates that the interaction between the two series leads
579 to an increase (decrease) in the entropy of the series p_j. Equivalently, it signifies that the *receiver*
580 series becomes more (less) unpredictable due to its interaction with the *transmitter* series. The
581 predictability of each time series is negatively correlated with the entropy.

597 While the information flow rate coefficients $T_{i \rightarrow j}$ were initially formulated for bi-variate systems
598 that involve two interacting time series, Liang has recently proved theoretically that the equations

Manuscript submitted to eLife

Box 3. The main properties of the information flow rate $T_{i \rightarrow j}$ are as follows:

1. In general, the correlation coefficients between $\hat{r}_{i,dj}$ are not symmetric under interchange of i and j, i.e., $\hat{r}_{i,dj} \neq \hat{r}_{j,di}$. The asymmetry of $\hat{r}_{i,dj}$ with respect to the interchange of i and j introduces directionality in the information flow rate coefficients, which implies that, in general, $T_{i \rightarrow j} \neq T_{j \rightarrow i}$.

2. For $i = j$, in light of $\hat{r}_{i,i} = 1$ both the numerator and the denominator on the right-hand side of *Equation 1* become zero. Thus, $T_{i \rightarrow i}$ is undetermined; however, this is not an issue, because the quantities of interest are the rates of information flow between different time series.

3. The presence of the coefficients $\hat{r}_{i,dj}$ and $\hat{r}_{j,dj}$ in the numerator on the right-hand side of *Equation 1* implies that $T_{i \rightarrow j}$ is proportional to the inverse of the finite difference time step, i.e., $\propto 1/k\Delta t$, where $k\Delta t$ is the time step used to calculate the time derivative (cf. *Equation 4*.)

---

above are also valid for N-variate, deterministic or stochastic systems (*Liang, 2016, 2018*). In addition, even though the estimator of $T_{i \rightarrow j}$ has been derived using the assumption of a linear system, it has been successfully applied to identify causal connections in nonlinear systems as well (*Liang, 2014, 2016*).

Normalized information flow rate

The information flow rate is based on the notion of information entropy. A positive $T_{2 \rightarrow 1}$ implies that the *transmitter* series p_2 increases the entropy of the *receiver* p_1, while a negative $T_{2 \rightarrow 1}$ implies the opposite. By comparing $T_{i \rightarrow j}$ with $T_{j \rightarrow i}$ (in the latter the roles of *transmitter* and *receiver* are reversed), we can determine which series transfers more information to the other series. However, this comparison does not reveal which of the two series is affected more due to its interaction with the other, because the coefficient does not account for the entropy change of each series due to the intrinsic evolution and possible stochastic effects. In order to quantify the impact of the entropy transferred to the *receiver* from a *transmitter* series, we need to know the extent to which the information transfer affects the predictability of the *receiver*, relative to all the other influences acting on the *receiver*.

The total rate of entropy change of p_j (*receiver*) depends not only on the information flow from p_i (*transmitter*), which is determined by the rate $T_{i \rightarrow j}$, but also on dH_j^*/dt and dH_j^s/dt. The term dH_j^*/dt (*intrinsic entropy rate*) represents the entropy rate of change due to the change of the phase space in the direction p_j. The term dH_j^s/dt (*noise-induced entropy rate*) represents the impact of stochastic effects in the dynamical system that underlies the evolution of p_j (*Liang, 2008*). Hence, as proposed by *Liang* (*2015*), a suitable normalization factor for the information flow rate from p_i to p_j is derived by adding the absolute values of the three rates that contribute to the total rate of entropy change of the *receiver* p_j, i.e.,

Manuscript submitted to eLife

Box 4. The main properties of the *normalized information flow rate* $\tau_{i \to j}$ are as follows:

1. The coefficient $\tau_{i \to j}$ is, in general, asymmetric, i.e., $\tau_{i \to j} \neq \tau_{j \to i}$ for $i \neq j$.
2. The $\tau_{i \to j}$ can take negative or positive values with magnitude less than one, i.e., $-1 \leq \tau_{i,j} \leq 1$. Positive values of $\tau_{i \to j}$ imply that the *transmitter* p_i tends to increase the entropy of the *receiver* p_j (i.e., it increases its uncertainty), while negative values imply that p_i reduces the entropy of p_j.
3. The $\tau_{i \to j}$ does not explicitly depend on the finite difference step $k\Delta t$. This is due to the fact that both the numerator and the denominator in *Equation 9* are proportional to $1/k\Delta t$.
4. The $\tau_{i \to j}$ measures the relative importance of the entropy change in the *receiver* series p_j due to its interaction with the *transmitter* p_i. The impact of p_i on p_j increases with the magnitude of $\tau_{i \to j}$.
5. The $\tau_{i \to j}$ is a relative measure which quantifies the information transfer from p_i to p_j with respect to the endogenous and noise-induced changes of the latter. However, it cannot be used to compare the information flow rate from p_i to p_j with that from p_j to p_i. This is due to the fact that the normalization of $\tau_{i \to j}$ depends on the entropy changes of p_j, while the normalization of $\tau_{j \to i}$ depends on the entropy changes of p_i. The comparison of the reverse information flows between p_i and p_j should thus be based on the non-normalized coefficients $T_{i \to j}$ and $T_{j \to i}$ (*Liang, 2015*).
6. The information flow rates (normalized and non-normalized) can be calculated without requiring (i) the estimation of conditional probability distributions (ii) stationarity assumptions (iii) Gaussian distribution of the fluctuations or (iv) a specific model structure.

$$Z_{i \to j} \equiv \left| T_{i \to j} \right| + \left| \frac{dH_j^*}{dt} \right| + \left| \frac{dH_j^s}{dt} \right|. \tag{8}$$

646 Based on *Equation 8*, $Z_{i \to j}$ is a non-negative number bounded from below by $|T_{i \to j}|$. In addition,

647 $Z_{i \to j}$ cannot be zero unless the rate of change of the intrinsic and stochastic entropy components

648 are zero. This can only happen if p_j is constant in time, which is not relevant for the EEG time

649 series. Thus, the *normalized information flow rate* from the *transmitter* p_i to the *receiver* p_j is defined

650 as (*Liang, 2015*)

$$\tau_{i \to j} = T_{i \to j} / Z_{i \to j}. \tag{9}$$

651 According to *Equation 9*, $\tau_{i \to j}$ measures the percentage of the total entropy rate of change for p_j

652 which is due to its interaction with p_i. The calculation of the terms which contribute to $Z_{i \to j}$ from

653 the data is explained in Appendix 1.

654 Based on the above analysis, the normalized information flow rate, $\tau_{i \to j}$, has several advantages

655 over the un-normalized coefficient, $T_{i \to j}$, the most important being that (1) $\tau_{i \to j}$ does not explicitly

656 depend on the finite difference step (item 3 in *Box 4*), and (2) it measures the importance of

657 information flow from the *transmitter* to the *receiver* (items 4 and 5 in *Box 4*). Hence, $\tau_{i \to j}$ is a suitable

658 measure for investigating patterns of information flow between different regions of the brain and

659 therefore for assessing effective connectivity.

Non-parametric testing of normalized information flow rate

661 To calculate $\tau_{i \to j}$ for each individual $l = 1, \dots L$, we use all the time points in the series $\{p_i^{(l)}(t_n)\}_{n=1}^{N_l}$, for

662 the source locations $i = 1, \dots, 15$. Each series represents the strength of the current dipole moment

663 at location i. All the time series for the same individual (indexed by l) have the same length N_l

664 which varies between 67845 and 114304 points.

665 In order to infer connectivity patterns, it is necessary to know if the estimated values $\tau_{i \to j}$ are

666 statistically significant. Each estimate of an inter-dipole $\tau_{i \to j}$ is a statistic, i.e., a random variable that

667 fluctuates between samples. If the sampling distribution of the statistic is known, the significance

668 of a particular estimate can be assessed using a suitably constructed parametric statistical test.

669 In the case of $T_{i \to j}$ such a test can be constructed (*Liang, 2014*). For $\tau_{i \to j}$, however, the sampling

670 distribution is not known. In this case, it is possible to apply *non-parametric permutation testing* in

671 the spirit used by Lachaux *et al.* to quantify the significance of phase locking values (*Lachaux et al.,*

672 *1999*; *Bastos et al., 2015*). The goal of non-parametric permutation testing is to determine the

673 probability that the observed test statistic could have been realized if the null hypothesis (i.e., zero

674 information flow) were true. This, in turn, allows us to conclude if an estimated information flow

675 rate is statistically significant: a very small probability (*p*-value) implies that the observed deviation

676 is not likely under the null hypothesis (*Maris and Oostenveld, 2007*; *Cohen, 2014*).

677 The test statistic that we use is the normalized information flow rate from series p_i to series p_j, for

678 $i \neq j = 1, \dots, 15$. The null hypothesis that we test is that there is no information flow between series

679 p_i and p_j. We generate $M_s = 1000$ randomized states $p'_{i[m]}(t_n)$, where $m = 1, \dots, M_s$ and $n = 1, \dots, N$,

680 from *each* transmitter time series p_i. Each randomized state is obtained by scrambling (by means of

681   random permutations) the N time points of p_i. The permutation destroys the temporal ordering

682   of p_i and consequently any patterns of information flow from $p'_{i[m]}(\cdot)$ to $p_j(\cdot)$. Hence, the estimated

683    $\tau_{i[m]\to j}$ values based on the shuffled time series p_i do not represent meaningful information flow.

684   The p-value of the statistic $\tau_{i\to j}$ is defined as the percentage of times — calculated over M_s

685   permutation states — that the randomized information flow rate $\tau_{i[m]\to j}$ is more extreme than $\tau_{i\to j}$

686   (i.e., larger than $\tau_{i\to j}$ if $\tau_{i\to j} > 0$ and smaller than $\tau_{i\to j}$ if $\tau_{i\to j} < 0$). A high p-value would indicate that

687   the null hypothesis cannot be rejected. In contrast, a low p-value would provide support for the

688   alternative hypothesis (i.e., that there is significant information flow from p_i to p_j). The observed

689   value $\tau_{i\to j}$ is then considered as statistically significant, if the respective p-value is below a specified

690   significance level (typically 0.1%–5%).

691   Based on all the simulations performed for the entire cohort of 32 individuals, we find that

692   the magnitude of the information flow rates between the randomly permuted *transmitter* current

693   dipoles and the *receiver* current dipoles are all contained in the interval $[-5.5, 5.0] \times 10^{-4}$. Turning to

694   the inter-dipole information flow rates calculated from the EEG data, we find that all except for 11

695   out of the 210×32=6720 dipole pairs show information flow rates outside the above interval. In fact,

696   the majority of the normalized information flow rates are two orders or more higher in magnitude.

697   Hence, given the size of the above confidence interval, we can conclude that most of the observed

698    $\tau_{i\to j}$ are statistically significant even at the $p = 0.1\%$ level.

699   The above result indicates a low-level global connectivity linking most of the brain regions in the

700   resting state. However, small normalized information flow rates, albeit statistically significant, imply

701   that the contribution of the respective entropy flow rate (information flow) from the *transmitter*

702   dipole to the *receiver* dipole is very small compared to the intrinsic entropy changes in the *receiver*

703   dipole. This argument motivates the introduction of an arbitrary threshold that can be used to

704   count the more important connections.

Impact of differencing scheme on connectivity

706   As stated following the definition of inter-dipole information flow rate, the estimation of the first-

707   order derivatives is based on finite differences (cf. *Equation 4*). The finite differencing, as shown

708   in *Equation 4*, can be accomplished by means of different time steps equal to $k\Delta t$. Typically, $k = 1$

709   or $k = 2$ is used (*Liang, 2014*). We have conducted our analysis with $k = 2$, since this choice tends to

710   reduce the impact of occasional large spikes (e.g., jumps) in the EEG time series on the information

711   flow rate. Using a larger value of k results in effective smoothing of the EEG time series which

712   encroaches on the upper end of the frequency band that is generally of interest in resting state

713   studies. Hence, we did not consider values of k higher than two.

714   We have experimented with synthetic data obtained from the simulation of two coupled stochas-

715   tic differential equations for which $T_{i\to j}$ admits explicit expressions (*Liang, 2014*). We used similar

716   length $N = 60000 - 80000$) for the synthetic time series as that of the EEG series and a number of

717   repetitions equal to the number of individuals in the study ($L = 32$). Our results show practically no

718   difference between the mean $T_{i\to j}$ estimated from the time series whether $k = 1$ or $k = 2$ is used.

719   In the case of the source-reconstructed EEG data, we repeated the entire analysis using $k = 1$.

720   This leads to fewer active connections, i.e., 1904 instead of 2821 for $k = 2$ shown in *Figure 8*. On the

other hand, the correlation coefficient between the spatial distribution of the frequency of active connections $n_{i \to j}(0.05)$ for $k = 1$ and for $k = 2$ is equal to 0.89. This indicates that the distribution of active connections is highly correlated between $k = 1$ and $k = 2$. Based on our arbitrary threshold $\tau_c = 0.05$, we determine 42 active connections ($\overline{\tau}_{i \to j} \geq \tau_c$) for the $k = 1$ scheme versus 92 active connections for the $k = 2$ scheme. In spite of the fact that fewer active connections appear for $k = 1$, the overall pattern of information flow, as delineated by the thirty connections with the highest $\overline{\tau}_{i \to j}$, remains unchanged.

Acknowledgments

References

Agcaoglu O, Miller R, Mayer AR, Hugdahl K, Calhoun VD. Lateralization of resting state networks and relationship to age and gender. NeuroImage. 2015; 104:310–325. doi: 10.1016/j.neuroimage.2014.09.001.

Baccalá LA, Sameshima K. Partial directed coherence: a new concept in neural structure determination. Biological cybernetics. 2001; 84(6):463–474. doi: 10.1007/PL00007990.

Barnett L, Barrett AB, Seth AK. Granger causality and transfer entropy are equivalent for Gaussian variables. Physical Review Letters. 2009 Dec; 103:238701. doi: 10.1103/PhysRevLett.103.238701.

Bastos AM, Schoffelen JM. A tutorial review of functional connectivity analysis methods and their interpretational pitfalls. Frontiers in Systems Neuroscience. 2015; 9. doi: 10.3389/fnsys.2015.00175.

Bastos AM, Vezoli J, Conrado AB, Schoffelen JM, Oostenveld R, Dowdall JR, De Weerd P, Kennedy H, Pascal F. Visual areas exert feedforward and feedback influences through distinct frequency channels. Neuron. 2015; 85(2):390–401. doi: 10.1016/j.neuron.2014.12.018.

BESA Wiki, BESA Research Montage Editor; 2018. http://wiki.besa.de/index.php?title=BESA_Research_Montage_Editor#Virtual_Standard_Montages, [Online; accessed 31-May-2018].

Blanco S, Garcia H, Quiroga RQ, Romanelli L, Rosso OA. Stationarity of the EEG series. IEEE Engineering in Medicine and Biology Magazine. 1995; 14(4):395–399. doi: 10.1109/51.395321.

Borich M, Babul AN, Yuan PH, Boyd L, Virji-Babul N. Alterations in resting-state brain networks in concussed adolescent athletes. Journal of Neurotrauma. 2015; 32(4):265–271. doi: 10.1089/neu.2013.3269.

Bossomaier T, Barnett L, Harré M, Lizier JT. An Introduction to Transfer Entropy: Information Flow in Complex Systems. Cham, Switzerland: Springer; 2016.

Bressler SL, Seth AK. Wiener–Granger causality: A well established methodology. NeuroImage. 2011; 58(2):323–329. doi: 10.1016/j.neuroimage.2010.02.059.

Chen Y, Rangarajan G, Feng J, Ding M. Analyzing multiple nonlinear time series with extended Granger causality. Physics Letters A. 2004; 324(1):26–35. doi: 10.1016/j.physleta.2004.02.032.

Cohen MX. Analyzing Neural Time Series Data: Theory and Practice. MIT Press; 2014.

Ding M, Chen Y, Bressler SL. Granger Causality: Basic Theory and Application to Neuroscience. In: *Handbook of Time Series Analysis* John Wiley & Sons, Ltd; 2006.p. 437–460. doi: 10.1002/9783527609970.ch17.

Emberson LL, Richards JE, Aslin RN. Top-down modulation in the infant brain: Learning-induced expectations rapidly affect the sensory cortex at 6 months. Proceedings of the National Academy of Sciences. 2015; 112(31):9585–9590. doi: 10.1073/pnas.1510343112.

Fair DA, Cohen AL, Dosenbach NUF, Church JA, Miezin FM, Barch DM, Raichle ME, Petersen SE, Schlaggar BL. The maturing architecture of the brain's default network. Proceedings of the National Academy of Sciences. 2008; 105(10):4028–4032. doi: 10.1073/pnas.0800376105.

Friston KJ. Functional and effective connectivity: a review. Brain Connectivity. 2011; 1(1):13–36. doi: 10.1089/brain.2011.0008.

Friston KJ. Functional and effective connectivity in neuroimaging: a synthesis. Human brain mapping. 1994; 2(1-2):56–78. doi: 10.1002/hbm.460020107.

Friston KJ, Harrison L, Penny W. Dynamic causal modelling. NeuroImage. 2003; 19(4):1273–1302. doi: 10.1016/S1053-8119(03)00202-7.

Gogtay N, Giedd JN, Lusk L, Hayashi KM, Greenstein D, Vaituzis AC, Nugent TF, Herman DH, Clasen LS, Toga AW, Rapoport JL, Thompson PM. Dynamic mapping of human cortical development during childhood through early adulthood. Proceedings of the National Academy of Sciences. 2004; 101(21):8174–8179. doi: 10.1073/pnas.0402680101.

Greicius MD, Supekar K, Menon V, Dougherty RF. Resting-state functional connectivity reflects structural connectivity in the default mode network. Cerebral Cortex. 2009; 19(1):72–78. doi: 10.1093/cercor/bhn059.

Gutzwiller MC. Chaos in Classical and Quantum Mechanics, vol. 1 of Interdisciplinary Applied Mathematics. New York: Springer; 1990.

Hesse W, Möller E, Arnold M, Schack B. The use of time-variant EEG Granger causality for inspecting directed interdependencies of neural assemblies. Journal of Neuroscience Methods. 2003; 124(1):27–44. doi: 10.1016/S0165-0270(02)00366-7.

Hillebrand A, Tewarie P, van Dellen E, Yu M, Carbo EWS, Douw L, Gouw AA, van Straaten ECW, Stam CJ. Direction of information flow in large-scale resting-state networks is frequency-dependent. Proceedings of the National Academy of Sciences. 2016; 113(14):3867–3872. doi: 10.1073/pnas.1515657113.

Hirayama J, Hyvärinen A, Kiviniemi V, Kawanabe M, Yamashita O. Characterizing variability of modular brain connectivity with constrained principal component analysis. PLoS ONE. 2016 12; 11(12):1–24. doi: 10.1371/journal.pone.0168180.

Horwitz B. The elusive concept of brain connectivity. NeuroImage. 2003; 19(2):466–470. doi: 10.1016/S1053-8119(03)00112-5.

Hutchison RM, Womelsdorf T, Allen EA, Bandettini PA, Calhoun VD, Corbetta M, Della Penna S, Duyn JH, Glover GH, Gonzalez-Castillo J, et al. Dynamic functional connectivity: promise, issues, and interpretations. NeuroImage. 2013; 80:360–378. doi: 10.1016/j.neuroimage.2013.05.079.

Kamiński M, Ding M, Truccolo WA, Bressler SL. Evaluating causal relations in neural systems: Granger causality, directed transfer function and statistical assessment of significance. Biological Cybernetics. 2001; 85(2):145–157. doi: 10.1007/s004220000235.

Kaplan AY, Fingelkurts AA, Fingelkurts AA, Borisov SV, Darkhovsky BS. Nonstationary nature of the brain activity as revealed by EEG/MEG: Methodological, practical and conceptual challenges. Signal Processing. 2005; 85(11):2190–2212. doi: 10.1016/j.sigpro.2005.07.010.

798 **Klonowski W**. Everything you wanted to ask about EEG but were afraid to get the right answer. Nonlinear
799   Biomedical Physics. 2009; 3(1):2. doi: 10.1186/1753-4631-3-2.

800 **Lachaux JP**, Rodriguez E, Martinerie J, Varela FJ. Measuring phase synchrony in brain signals. Human Brain
801   Mapping. 1999; 8(4):194–208. doi: 10.1002/(SICI)1097-0193(1999)8:4\%3C194::AID-HBM4\%3E3.0.CO;2-C.

802 **Lebel C**, Beaulieu C. Longitudinal development of human brain wiring continues from childhood into adulthood.
803   Journal of Neuroscience. 2011; 31(30):10937–10947. doi: 10.1523/JNEUROSCI.5302-10.2011.

804 **Li J**, Wang ZJ. Controlling the false discovery rate of the association/causality structure learned with the PC
805   algorithm. Journal of Machine Learning Research. 2009 Jun; 10:475–514.

806 **Liang XS**. Information flow within stochastic dynamical systems. Physical Review E. 2008; 78(3):031113. doi:
807   10.1103/PhysRevE.78.031113.

808 **Liang XS**. The Liang-Kleeman information flow: Theory and applications. Entropy. 2013; 15(1):327–360. doi:
809   10.3390/e15010327.

810 **Liang XS**. Local predictability and information flow in complex dynamical systems. Physica D: Nonlinear
811   Phenomena. 2013; 248:1–15. doi: 10.1016/j.physd.2012.12.011.

812 **Liang XS**. Unraveling the cause-effect relation between time series. Physical Review E. 2014; 90(5):052150. doi:
813   10.1103/PhysRevE.90.052150.

814 **Liang XS**. Normalizing the causality between time series. Physical Review E. 2015; 92(2):022126. doi:
815   10.1103/PhysRevE.92.022126.

816 **Liang XS**. Information flow and causality as rigorous notions ab initio. Physical Review E. 2016; 94(5):052201.
817   doi: 10.1103/PhysRevE.94.052201.

818 **Liang XS**. Causation and information flow with respect to relative entropy. Chaos: An Interdisciplinary Journal
819   of Nonlinear Science. 2018; 28(7):075311. doi: 10.1063/1.5010253.

820 **Liang XS**, Kleeman R. Information Transfer between Dynamical System Components. Physica Review Letters.
821   2005; 95:244101. doi: 10.1103/PhysRevLett.95.244101.

822 **Lin P**, Yang Y, Gao J, De Pisapia N, Ge S, Wang X, Zuo CS, Levitt JJ, Niu C. Dynamic default mode network across
823   different brain states. Scientific Reports. 2017; 7:46088. doi: 10.1038/srep46088.

824 **Lindquist MA**. The statistical analysis of fMRI data. Statistical Science. 2008; 23(4):439–464. doi: 10.1214/09-
825   STS282.

826 **Liu Q**, Farahibozorg S, Porcaro C, Wenderoth N, Mantini D. Detecting large-scale networks in the human
827   brain using high-density electroencephalography. Human Brain Mapping. 2017; 38(9):4631–4643. doi:
828   10.1002/hbm.23688.

829 **Liu Y**, Aviyente S. Quantification of effective connectivity in the brain using a measure of directed information.
830   Computational and Mathematical Methods in Medicine. 2012; 2012. doi: 10.1155/2012/635103.

831 **Marinazzo D**, Liao W, Chen H, Stramaglia S. Nonlinear connectivity by Granger causality. NeuroImage. 2011;
832   58(2):330–338. doi: 10.1016/j.neuroimage.2010.01.099.

833 **Maris E**, Oostenveld R. Nonparametric statistical testing of EEG- and MEG-data. Journal of Neuroscience
834   Methods. 2007; 164(1):177–190. doi: 10.1016/j.jneumeth.2007.03.024.

835 **Marshall WJ**, Lackner CL, Marriott P, Santesso DL, Segalowitz SJ. Using phase shift Granger causality
836   to measure directed connectivity in EEG recordings. Brain Connectivity. 2014; 4(10):826–841. doi:
837   10.1089/brain.2014.0241.

838 **McLntosh AR**, Gonzalez-Lima F. Structural equation modeling and its application to network analysis in
839   functional brain imaging. Human Brain Mapping. 1994; 2(1-2):2–22. doi: 10.1002/hbm.460020104.

840 **Michels L**, Muthuraman M, Lüchinger R, Martin E, Anwar AR, Raethjen J, Brandeis D, Siniatchkin M. Develop-
841   mental changes of functional and directed resting-state connectivities associated with neuronal oscillations in
842   EEG. NeuroImage. 2013; 81:231–242. doi: 10.1016/j.neuroimage.2013.04.030.

843 **Mill RD**, Bagic A, Bostan A, Schneider W, Cole MW. Empirical validation of directed functional connectivity.
844   NeuroImage. 2017; 146:275–287. doi: 10.1016/j.neuroimage.2016.11.037.

845 **Miskovic V**, Ma X, Chou CA, Fan M, Owens M, Sayama H, Gibb BE. Developmental changes in spontaneous
846   electrocortical activity and network organization from early to late childhood. NeuroImage. 2015; 118:237–247.
847   doi: 10.1016/j.neuroimage.2015.06.013.

848 **Muetzel RL**, Blanken LME, Thijssen S, van der Lugt A, Jaddoe VWV, Verhulst FC, Tiemeier H, White T. Resting-
849   state networks in 6-to-10 year old children. Human Brain Mapping. 2016; 37(12):4286–4300. doi:
850   10.1002/hbm.23309.

851 **Muthuraman M**, Moliadze V, Mideksa KG, Anwar AR, Stephani U, Deuschl G, Freitag CM, Siniatchkin M. EEG-MEG
852   integration enhances the characterization of functional and effective connectivity in the resting state network.
853   PLoS ONE. 2015; 10(10):e0140832. doi: 10.1371/journal.pone.0140832.

854 **Paus T**. Mapping brain maturation and cognitive development during adolescence. Trends in Cognitive Sciences.
855   2005; 9(2):60–68. doi: 10.1016/j.tics.2004.12.008.

856 **Perrin F**, Pernier J, Bertrand O, Echallier JF. Spherical splines for scalp potential and current density mapping. Elec-
857   troencephalography and Clinical Neurophysiology. 1989; 72(2):184–187. doi: 10.1016/0013-4694(89)90180-6.

858 **Porter S**, Torres IJ, Panenka W, Rajwani Z, Fawcett D, Hyder A, Virji-Babul N. Changes in brain-behavior relation-
859   ships following a 3-month pilot cognitive intervention program for adults with traumatic brain injury. Heliyon.
860   2017; 3(8):e00373. doi: 10.1016/j.heliyon.2017.e00373.

861 **Raichle ME**, MacLeod AM, Snyder AZ, Powers WJ, Gusnard DA, Shulman GL. A default mode of brain function.
862   Proceedings of the National Academy of Sciences. 2001; 98(2):676–682. doi: 10.1073/pnas.98.2.676.

863 **Raichle ME**, Mintun MA. Brain work and brain imaging. Annual Reviews of Neuroscience. 2006; 29:449–476.
864   doi: 10.1146/annurev.neuro.29.051605.112819.

865 **Roebroeck A**, Formisano E, Goebel R. Mapping directed influence over the brain using Granger causality and
866   fMRI. NeuroImage. 2005; 25(1):230–242. doi: https://doi.org/10.1016/j.neuroimage.2004.11.017.

867 **Rotem-Kohavi N**, Hilderman CGE, Liu A, Makan N, Wang JZ, Virji-Babul N. Network analysis of perception-action
868   coupling in infants. Frontiers in Human Neuroscience. 2014; 8:209. doi: 10.3389/fnhum.2014.00209.

869 **Rotem-Kohavi N**, Oberlander TF, Virji-Babul N. Infants and adults have similar regional functional brain
870   organization for the perception of emotions. Neuroscience Letters. 2017; 650(Supplement C):118–125. doi:
871   10.1016/j.neulet.2017.04.031.

872 **Rubinov M**, Sporns O. Complex network measures of brain connectivity: Uses and interpretations. NeuroImage.
873   2010; 52(3):1059–1069. doi: 10.1016/j.neuroimage.2009.10.003.

874 **Sakkalis V**. Review of advanced techniques for the estimation of brain connectivity measured with EEG/MEG.
875   Computers in Biology and Medicine. 2011; 41(12):1110–1117. doi: 10.1016/j.compbiomed.2011.06.020.

876 **Salvador R**, Anguera M, Gomar J, Bullmore E, Pomarol-Clotet E. Conditional mutual information maps as
877   descriptors of net connectivity levels in the brain. Frontiers in Neuroinformatics. 2010; 4:115–123. doi:
878   10.3389/fninf.2010.00115.

Scherg M, Ille N, Bornfleth H, Berg P. Advanced tools for digital EEG review: Virtual source montages, whole-head mapping, correlation, and phase analysis. Journal of Clinical Neurophysiology. 2002; 19(2):91–112.

Schreiber T. Measuring information transfer. Physical Review Letters. 2000; 85(2):461–464. doi: 10.1103/Phys-RevLett.85.461.

Seth A. Granger causality. Scholarpedia. 2007; 2(7):1667. revision #91329.

Seth AK, Barrett AB, Barnett L. Granger causality analysis in neuroscience and neuroimaging. Journal of Neuroscience. 2015; 35(8):3293–3297. doi: 10.1523/JNEUROSCI.4399-14.2015.

Shaw P, Kabani NJ, Lerch JP, Eckstrand K, Lenroot R, Gogtay N, Greenstein D, Clasen L, Evans A, Rapoport JL, Giedd JN, Wise SP. Neurodevelopmental trajectories of the human cerebral cortex. Journal of Neuroscience. 2008; 28(14):3586–3594. doi: 10.1523/JNEUROSCI.5309-07.2008.

Shovon MHI, Nandagopal DN, Vijayalakshmi R, Du JT, Cocks B. Transfer entropy and information flow patterns in functional brain networks during cognitive activity. In: *International Conference on Neural Information Processing* Springer; 2014. p. 1–10.

Smit DJA, Boersma M, Schnack HG, Micheloyannis S, Boomsma DI, Pol HEH, Stam CJ, de Geus EJC. The brain matures with stronger functional connectivity and decreased randomness of its network. PLoS ONE. 2012; 7(5):e36896. doi: 10.1371/journal.pone.0036896.

Snyder AZ, Raichle ME. A brief history of the resting state: the Washington University perspective. NeuroImage. 2012; 62(2):902–910. doi: 10.1016/j.neuroimage.2012.01.044.

Sporns O. Networks of the Brain. MIT Press; 2011.

Stam CJ, Van Straaten ECW. The organization of physiological brain networks. Clinical Neurophysiology. 2012; 123(6):1067–1087. doi: 10.1016/j.clinph.2012.01.011.

Taylor MJ, Khan SC. Top-down modulation of early selective attention processes in children. International Journal of Psychophysiology. 2000; 37(2):135–147. doi: 10.1016/S0167-8760(00)00084-2.

Toga AW, Thompson PM, Mori S, Amunts K, Zilles K. Towards multimodal atlases of the human brain. Nature Reviews Neuroscience. 2006; 7(12):952–966. doi: 10.1038/nrn2012.

Vicente R, Wibral M, Lindner M, Pipa G. Transfer entropy—a model-free measure of effective connectivity for the neurosciences. Journal of Computational Neuroscience. 2011; 30(1):45–67. doi: 10.1007/s10827-010-0262-3.

Van de Ville D, Britz J, Michel CM. EEG microstate sequences in healthy humans at rest reveal scale-free dynamics. Proceedings of the National Academy of Sciences. 2010; 107(42):18179–18184. doi: 10.1073/pnas.1007841107.

Virji-Babul N, Hilderman CGE, Makan N, Liu A, Smith-Forrester J, Franks C, Wang ZJ. Changes in functional brain networks following sports-related concussion in adolescents. Journal of Neurotrauma. 2014; 31(23):1914–1919. doi: /10.1089/neu.2014.3450.

Yuan H, Ding L, Zhu M, Zotev V, Phillips R, Bodurka J. Reconstructing large-scale brain resting-state networks from high-resolution EEG: spatial and temporal comparisons with fMRI. Brain Connectivity. 2016; 6(2):122–135. doi: 10.1089/brain.2014.0336.

Table 1. List of the most active connections based on the ensemble mean of the normalized information flow rate, $\tau_{i \rightarrow j}$. All $\tau_{i \rightarrow j}$ listed exceed the threshold $\tau_c = 0.05$. The connections listed are included among those shown in the bottom matrix plot of *Figure 1*. The last column in the table reports the polarization which is equal to the sum of the signs of $\tau_{i \rightarrow j}$ over the individuals as a percentage of the number of individuals in the study ($L = 32$) [see *Equation 6*].

	From	To	Mean $\tau_{i \rightarrow j}$	Polarization
1	FL	TAL	1.164062e-01	100
2	FL	FpM	1.062701e-01	100
3	TAL	CL	1.048785e-01	100
4	FM	FR	1.039752e-01	94
5	FL	FM	1.023856e-01	100
6	TPL	CL	9.902969e-02	100
7	TAL	FL	9.789913e-02	100
8	TAR	FR	9.752876e-02	100
9	FpM	FL	9.738423e-02	100
10	FL	CL	9.737341e-02	100
11	FR	TAR	9.643028e-02	100
12	FM	FL	9.108766e-02	100
13	FpM	FM	8.720060e-02	94
14	FM	CL	8.698357e-02	94
15	TAL	TPL	8.462667e-02	94
16	FpM	TAL	8.422089e-02	88
17	PM	OpM	8.336186e-02	100
18	FpM	FR	8.322882e-02	94
19	FM	CM	8.248654e-02	100
20	FpM	CL	8.198255e-02	100
21	FR	FM	8.095464e-02	94
22	FM	FpM	8.034528e-02	100
23	CM	FM	8.017243e-02	100
24	PL	OpM	7.770022e-02	100
25	FL	FR	7.733949e-02	100
26	PR	OpM	7.503928e-02	100
27	CM	CL	7.419229e-02	100
28	TPL	TAL	7.341683e-02	100
29	TAR	TPR	7.276059e-02	100
30	FpM	TAR	7.214605e-02	94

Table 2. List of the 15 brain regions used in EEG source space reconstruction in BESA.

Source Dipole Label	Brain Region
FL	Frontal, left hemisphere
FpM	Fronto-polar midline
FR	Frontal, right hemisphere
FM	Frontal midline
CL	Central, left hemisphere
CM	Central midline
CR	Central, right hemisphere
TPL	Posterior temporal, left hemisphere
TAL	Anterior temporal, left hemisphere
TAR	Anterior temporal, right hemisphere
TPR	Posterior temporal, right hemisphere
PM	Parietal midline
PL	Parietal, left hemisphere
PR	Parietal, right hemisphere
OpM	Occipital-polar midline

Manuscript submitted to eLife

Appendix 1

Herein we show how the two entropic components involved, in addition to $|T_{i \to j}|$, in the normalization term $Z_{i \to j}$, can be estimated from the data. Analysis based on the theory of dynamical systems leads to the following expressions for the rates of change of the entropic components H_j^* and H_j^s (**Liang, 2008**)

$$\frac{dH_j^*}{dt} = p_{i,j},$$ (10a)

$$\frac{dH_j^s}{dt} = \frac{\Delta t}{2\widehat{C}_{j,j}} \left[\widehat{C}_{dj,dj} + p_{i,j}^2 \widehat{C}_{j,j} + q_{i,j}^2 \widehat{C}_{i,i} - 2p_{i,j}\widehat{C}_{dj,j} - 2q_{i,j}\widehat{C}_{dj,i} + 2p_{i,j}q_{i,j}\widehat{C}_{j,i} \right]$$

$$= \frac{\Delta t}{2} \left[\widehat{r}_{dj,dj} + p_{i,j}^2 + q_{i,j}^2 \frac{\widehat{\sigma}_i^2}{\widehat{\sigma}_j^2} - 2p_{i,j}\widehat{r}_{dj,j} - 2q_{i,j}\widehat{r}_{dj,i}\frac{\widehat{\sigma}_i}{\widehat{\sigma}_j} + 2p_{i,j}q_{i,j}\widehat{r}_{j,i}\frac{\widehat{\sigma}_i}{\widehat{\sigma}_j} \right],$$ (10b)

where the entropy transfer elements $p_{i,j}$, $q_{i,j}$ are given by the following functions of the inter-dipole covariance coefficients

$$p_{i,j} = \frac{\widehat{C}_{i,i}\widehat{C}_{j,dj} - \widehat{C}_{j,i}\widehat{C}_{i,dj}}{\widehat{C}_{j,j}\widehat{C}_{i,i} - \widehat{C}_{j,i}^2},$$

$$q_{i,j} = \frac{-\widehat{C}_{j,i}\widehat{C}_{j,dj} + \widehat{C}_{j,j}\widehat{C}_{i,dj}}{\widehat{C}_{j,j}\widehat{C}_{i,i} - \widehat{C}_{j,i}^2}, \quad i,j = 1, \dots, L.$$

Using the definition in **Equation 2** for the correlation coefficient and the definition in **Equation 3** for the cross-correlation coefficient, the elements $p_{i,j}$ and $q_{i,j}$ can be expressed using correlation coefficients r instead of inter-dipole covariances C as follows (for $i, j = 1, \dots, N_s$):

$$p_{i,j} = \frac{\widehat{r}_{j,dj} - \widehat{r}_{j,i}\widehat{r}_{i,dj}}{1 - \widehat{r}_{j,i}^2},$$ (11a)

$$q_{i,j} = \frac{\frac{\widehat{C}_{i,dj}}{\widehat{C}_{i,i}} - \frac{\widehat{C}_{j,i}}{\widehat{C}_{i,i}}\widehat{r}_{j,dj}}{1 - \widehat{r}_{j,i}^2} = \frac{\widehat{\sigma}_j}{\widehat{\sigma}_i}\frac{\left(\widehat{r}_{i,dj} - \widehat{r}_{j,i}\widehat{r}_{j,dj}\right)}{1 - \widehat{r}_{j,i}^2}.$$ (11b)